Robust anti-tumor immunity through the integration of targeted lipid nanoparticle-based mRNA nanovaccines with PD-1/PD-L1 blockade

Chengyan Jin [a], Yan Zhang [a], Baofeng Li [a], Tianci Gao [b], Bin Wang [a], Peiyan Hua [a,*]

[a] *Department of Thoracic Surgery, The Second Hospital of Jilin University, Changchun, Jilin Province, 130022, China*
[b] *College of Clinical Medicine, Jiamusi University, Jiamusi, Heilongjiang Province, 154007, China*

ARTICLE INFO

ABSTRACT

Tumor mRNA vaccines present a personalized approach in cancer immunotherapy, encoding distinct tumor antigens to evoke robust immune responses and offering the potential against emerging tumor variants. Despite this, the clinical advancement of tumor mRNA vaccines has been hampered by their limited delivery capacity and inefficient activation of antigen-presenting cells (APCs). Herein, we employed microfluidics technology to engineer mannose-modified lipid-based nanovaccines for specifically targeting APCs. The encapsulation process efficiently entrapped the cyclic guanosine monophosphate-adenosine monophosphate (cGAMP) agonist along with mRNA encoding antigens. The targeted nanovaccines (TNVs) exhibited a narrow particle size distribution, ensuring consistent and efficient delivery. These TNVs significantly enhanced gene expression of mRNA, facilitating antigen presentation and immune activation. When compared to non-targeted nanovaccines, TNVs outperformed in terms of antigen presentation and immune activation. Furthermore, the combination of anti-PD-L1 antibodies with TNVs elicited a synergistic anti-tumor effect. This was attributed to the anti-PD-L1 antibodies' ability to overcome the immune suppression of tumor cells. Our findings suggest that the combination treatment elicited the most robust anti-tumor immune activation and immune memory effect. These results indicate that integrating tumor mRNA vaccines with immune checkpoint inhibitors or other immunostimulatory agents may be crucial for enhancing the immune response.

1. Introduction

Malignant tumor is a serious threat to human life and health, its morbidity and mortality are high, and it is one of the main public health problems facing the world [1]. Tumor immunotherapy has emerged as a promising therapeutic approach, as it stimulates and enhances the body's immune response to specifically target and eliminate tumor cells. This method holds significant promise following surgical, chemical, and radiological treatments [2]. By harnessing the body's own immune system, immunotherapy aims to eliminate tumor cells, effectively halt tumor growth, and generate immune memory against future tumor recurrences or metastases, potentially leading to complete tumor eradication [3,4]. Currently, adaptive T-cell transfer therapy, immune checkpoint inhibitors, tumor vaccines, and other immunotherapy drugs have demonstrated promising results in the treatment of melanoma, non-small cell lung cancer, and other tumor types [5]. However, tumor immunotherapy still faces numerous challenges, including the release of tumor cell antigens, their presentation by antigen-presenting cells, T lymphocyte activation, their transport to tumor sites, infiltration within tumor tissue, recognition of tumor antigens within the tumor microenvironment, and ultimately, the elimination of tumor cells [6,7]. Among these, activating cytotoxic T lymphocytes and overcoming the immunosuppressive tumor microenvironment are particularly crucial.

Tumor vaccines stimulate the immune system to generate active, specific responses against tumor cells. This is achieved through the presentation of tumor cell cleavage products, tumor-specific antigens, tumor-associated antigens, and tumor polypeptides [8–10]. This immune response aims to halt or eradicate tumor growth, recurrence, and metastasis. Depending on the delivery vectors employed, tumor vaccines are categorized into various types: cell-based vaccines, such as tumor cell vaccines, dendritic cell vaccines, and genetically modified cell vaccines; viral vaccines; protein/peptide vaccines; DNA vaccines; and RNA vaccines [11,12]. Of these, messenger RNA (mRNA) vaccines have emerged as a promising avenue due to their high safety, effectiveness, and yield profile. This success, demonstrated in the development of the novel coronavirus vaccine, has sparked interest in the application of

* Corresponding author.
  E-mail address: huapeiyan@jlu.edu.cn (P. Hua).

mRNA technology for tumor vaccines [13–17]. Clinical trials with mRNA tumor vaccines have demonstrated durable objective responses in cancer patients, without significant toxic side effects. This suggests the potential of mRNA tumor vaccines in cancer therapy [18]. The success of mRNA tumor vaccines hinges on the selection of tumor-specific antigens, immunologic adjuvants, and efficient mRNA delivery systems [19]. With the rapid advancements in biomedical and molecular biology technologies, progress in identifying tumor-specific antigens and neoantigens for clinical trials has been significant [20]. Currently, the cellular immunity induced by aluminum salt adjuvants, commonly used in human vaccines, is limited and insufficient for meeting the demands of vaccine development. Cyclic guanosine monophosphate-adenosine monophosphate (cGAMP), a recently discovered mammalian second messenger, has the potential to activate the endoplasmic reticulum-resident STING pathway, stimulating innate immunity and the expression of MHCII antigens on immature dendritic cells [21]. Furthermore, cGAMP possesses the remarkable ability to augment the secretion of cytokines and chemokines, thereby enhancing the immunogenicity of vaccines and specifically amplifying the T cell response. This makes it a promising contender for the next generation of cancer vaccine adjuvants [22]. An efficient delivery mechanism is crucial for the effective transportation of mRNA, ensuring its efficient endocytosis by antigen-presenting cells. This, in turn, promotes the escape of mRNA endosomes, facilitates the translation and encoding of proteins, and ultimately triggers both humoral and cellular immune responses within the body [23]. The current array of delivery systems encompasses viral vector-based methods, lipid nanoparticles (LNPs), polymer-based systems, hybrid vectors, and polypeptide-based delivery, among others. Notably, the delivery system rooted in liposomes and their derivatives has emerged as the most widespread and effective approach [24].

The tumor immune microenvironment is a local homeostatic milieu that fosters tumor growth and reproduction. This intricate ecosystem is comprised of tumor cells alongside stromal cells, including immune cells, inflammatory cells, and fibroblasts [25]. Research has revealed that the tumor immune microenvironment, shaped by immune cells, cell surface receptors, and associated cytokines, thwarts the body's immune system's ability to specifically recognize tumor cells, leading to immune evasion. Consequently, this process accelerates tumor growth, proliferation, recurrence, and metastasis [26]. The tumor immunosuppressive microenvironment is both complex and dynamic, facilitating the immune evasion of tumor cells. A significant role in this process is played by immunosuppressive cells, including Treg cells, bone marrow-derived suppressive cells, and tumor-associated macrophages [27]. Furthermore, immune-related inhibitory cytokines and molecules secreted by tumor cells contribute to the establishment of the immunosuppressive microenvironment. Tumor cells cunningly evade the immune surveillance of the body through an intricate network structure, which grants them the ability to proliferate, replicate, migrate, infiltrate, and ultimately metastasize [28]. Immune checkpoint inhibitor (ICI) therapy has emerged as one of the most widely utilized tumor immunotherapy approaches, aimed at reshaping the immunosuppressive microenvironment by blocking immune checkpoints [29–31]. In 2011, the FDA approved the first inhibitor specifically targeting the immune checkpoint CTLA-4, the monoclonal drug ipilimumab, for use in immunotherapy against advanced melanoma [32]. In 2014, Nivolumab, the world's first PD-1 inhibitor, was launched in Japan for the immunotherapy of melanoma, recurrent head and neck cancer, advanced non-small cell lung cancer and other cancers, marking a new era in tumor immunotherapy [33]. Tumor immunotherapy, whether administered as monotherapy or combination therapy using immune checkpoint inhibitors, holds immense promise as one of the most cutting-edge fields in anti-tumor therapy.

In this study, we have successfully developed a promising nanovaccine platform that simultaneously delivers a synthetic mRNA antigen along with a cGAMP adjuvant to stimulate robust adaptive immune responses (Scheme 1). To enhance the targeting efficiency of antigen-presenting cells (APCs), SM102-based LNPs were optimized by incorporating mannose-PEG-lipid (Man-PEG2k-DSPE). These targeted LNPs effectively facilitate phagocytosis by APCs and promote the expression of tumor antigens. The tumor nanovaccines were meticulously crafted by co-encapsulating ovalbumin mRNA (mOVA) and cGAMP adjuvant within the targeted LNPs using microfluidic control technology. Furthermore, to modulate the immunosuppressive tumor microenvironment (TME), anti-PD-L1 antibody was employed to reverse the immunosuppressive state of the TME, thereby enhancing the activation of cytotoxic T lymphocytes. This integrated strategy of mRNA nanovaccines and anti-PD-L1 blockade exhibited remarkable antigen expression, robust APC activation, and augmented T cell response, leading to a potentiated anti-tumor immune response. This approach represents a highly effective combined anti-tumor therapy.

2. Experimental methods

2.1. Materials

Heptadecan-9-yl 8-((2-hydroxyethyl) (6-oxo-6-(undecyloxy) hexyl) amino) octanoate (SM102), 1.2-distearoyl-*sn*-glycero-3-phosphocholine (DSPC), murine interleukin4 (IL-4), Cholesterol, cGAMP, 3-(4,5-dimethylthiazol-2-yl)-2,5 diphenyl tetrazolium bromide (MTT), lipopolysaccharide (LPS), 1.2-dimyristoyl-rac-*glycero*-3-methoxypolyethylene glycol-2000 (DMG-PEG2000), and murine granulocyte-macrophage colony-stimulating factor (GM-CSF) were purchased from Sigma-Aldrich (St. Louis, MI, USA). DSPE-PEG2000-mannose was purchased from Biochempeg. Lipofectamine™ MessengerMAX™ (MAX) mRNA transfection reagent was ordered from Thermo Fisher Scientific (Sunnyvale, CA, USA). Firefly luciferase mRNA (mFluc), enhanced green fluorescence protein mRNA (EGFP-mRNA), and ovalbumin mRNA (mOVA) were purchased from TriLink BioTechnologies (California, USA). Universal Virus Concentration Kits and D-Luciferin potassium salt (luciferase substrate) were purchased from Beyotime Biotechnology (Beijing, China). Luciferase assay kit was ordered from Promega (Madison, Wisconsin, USA). Lipofectamin™2000 transfection reagent, BCA protein assay kit, total RNA extraction kit, reverse transcription kit, qRT-PCR detection kit, and Quant-iT RiboGreen RNA quantify kit were purchased from Thermo Fisher Scientific (Massachusetts, USA). Ultra-filtration centrifugal tube (MWCO, 100 kDa) was obtained from Millipore (USA). A anti-PD-L1 recombinant monoclonal antibody was purchased from BioXcell, Inc. (West Lebanon, USA). All the plasmids were constructed by Wuhan Miaoling Biotechnology Co., Ltd. (Wuhan, China). All other flow fluorescent antibodies were ordered from eBioscience (California, USA). All the solvents are analytical and purchased from Sinopharm (Beijing, China).

2.2. Preparation of targeted nanovaccines

The targeted nanovaccines were meticulously crafted using a microfluidic technique. Briefly, the ingredients SM-102, DSPC, Cholesterol, DSPE-PEG2000-Mannose, and DMG-PEG2000 were dissolved in absolute ethanol in precise molar ratios of 50:10:38.5:0.3:1.2, respectively, to form the targeted lipid nanoparticles (TLNP) delivery system for preparation of targeted nanovaccines. For the non-targeted LNP, SM-102, DSPC, Cholesterol, and DMG-PEG2000 were dissolved in ethanol in the molar ratios of 50:10:38.5:1.5. Prior to the preparation of the LNP-mRNA nanoparticles, the mRNAs were dissolved in RNAase-free sodium citrate buffer maintained at pH 4 and a concentration of 50 mM. Subsequently, the LNP-mRNA nanoparticles were obtained via a microfluidic preparation equipment (MPE-L2, Aitesen, China). For the creation of TLNP-mRNA/cGAMP nanovaccines and LNP-mRNA/cGAMP, the mRNA and cGAMP were combined in a final mass ratio of 5:1. The liquid mixtures were blended in a volume ratio of 1:3, with the ethanol phase and aqueous phase flowing at rates of 4 mL/min and 12
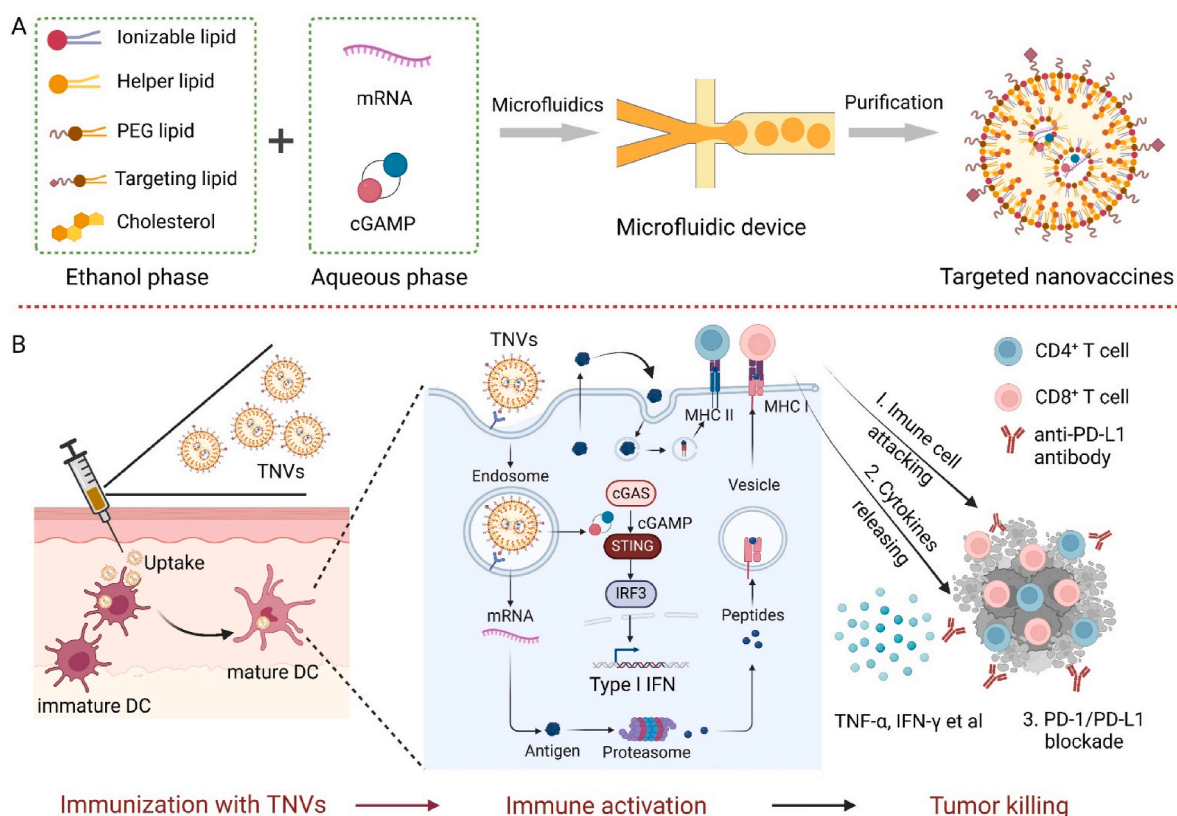
Scheme 1. Schematic illustration for anti-tumor immunity through the integration of targeted lipid nanoparticle-based mRNA nanovaccines with PD-1/PD-L1 blockade. (A) Preparation route of targeted nanovaccines using microfluidic control technology. (B) Schematic route of immunization and immune activation of targeted nanovaccines, and their anti-tumor immune killing effect of combined PD-1/PD-L1 blockade. Part image elements from Biorender.com.

mL/min, respectively. The prefabricated nanovaccines were purified using ultrafiltration tubes with a cutoff molecular weight of 100 kDa at a speed of 8000×*g*. They were further diluted in sterile buffer consisting of 10 mM Tris-HCl, 10.7 mM sodium acetate, and 87 mg/mL saccharose in MilliQ water, maintained at pH 7.5. The resulting nanovaccines were harvested and stored at 4 °C for future use.

2.3. Characterization of nanovaccines

The Quant-iT RiboGreen RNA kit was utilized to assess the encapsulation efficiency of mRNA within nanovaccines. By referencing the standard curve, the concentration of free mRNA was determined, and subsequently, the manufacturer's instructions were followed to obtain the final encapsulation efficiency. The dynamic light scattering technique was employed to verify the particle size, polydispersity index, and zeta potentials of the nanovaccines, all under conditions of a constant mRNA concentration of 10 μg/mL. Additionally, the surface morphology of the nanovaccines was examined using a scanning electron microscopy (SEM, SU7000, Hitachi, Japan) and transmission electron microscopy (TEM, FEI Tecnai G2 Spirit BioTwin, USA). To evaluate the stability of the nanovaccines, they were stored at 4 °C for various durations, including 0, 1, 3, 5, 7, 14, and 28 days. At these designated time points, the particle sizes and drug encapsulation efficiencies (EE%) of the nanovaccines were assayed to assess their stability. The EE% was calculated using the following formula:

$$\text{mRNA EE\%} = \frac{\text{Total mRNA} - \text{Unencapsulated mRNA}}{\text{Total mRNA}} \times 100$$

2.4. Biocompatibility study in bone marrow-derived dendritic cells (BMDCs)

BMDCs were extracted and subsequently employed in the assessment of the biocompatibility of the prepared nanovaccines. Briefly, the BMDCs were meticulously isolated from the femurs of C57BL/6 male mice aged 6 weeks, adhering to the procedures outlined in the literature [34]. These cells were then cultured in Dulbecco's Modified Eagle Medium (DMEM), enriched with high glucose, 10 % fetal bovine serum, 20 ng/mL GM-CSF, 10 ng/mL IL-4, and 1 % streptomycin-penicillin antibiotic to ensure optimal growth conditions. For the biocompatibility study, the cells were seeded onto 96-well plates at a density of 1.0×10^4 cells per well. The nanovaccines were introduced to the wells at various mRNA concentrations ranging from 2.5 to 25 μg/mL. After a 24-h incubation period, 20 μL of MTT solution (dissolved at 5 mg/mL in PBS buffer) was added to each well, replacing the fresh medium. After a further 4 h, the medium was gently discarded, and 200 μL of DMSO was added. Subsequently, the absorption value at 490 nm was measured using a microplate reader. The cell viability was calculated meticulously, adhering strictly to the manufacturer's protocols, ensuring accurate and reliable results.

2.5. Intracellular uptake and endosome escape in BMDCs

Immature BMDCs were gently seeded into 6-well plates, maintaining a cell density of 1.0×10^6 cells per well. Following an overnight incubation, Cy5-mRNA, Cy5-mRNA loaded LNP, and Cy5-mRNA loaded TLNP were delicately introduced into the wells and incubated for 4 h, ensuring a final Cy5-mRNA concentration of 1 μg/mL. Different molar ratios of DSPE-PEG2000-Mannose and DMG-PEG2000 were screened, including 0.1:1.4, 0.2:1.3, 0.3:1.2, 0.4:1.1, and 0.5:1.0. Subsequently, the cells were meticulously collected, centrifuged at 1000 rpm, and

washed three times with cold PBS buffer to eliminate any residual extracellular components. The harvested cells were then subjected to a flow cytometer (Guava easycyte 6-2L, Luminex, USA) for detailed analysis, with the data meticulously processed by Flowjo software. The mannose receptor expression in BMDCs and LLC-OVA cells was measured by incubation with PE-CD11c and APC-labeled anti-MR antibody for 30 min at 4 °C. The cells were collected and analyzed via flow cytometry. To validate the targeted endocytosis mechanism of the nanovaccines, we conducted a mannose competition experiment. Prior to the introduction of the LNP/Cy5-mRNA and TLNP/Cy5-mRNA nanovaccines, BMDCs were incubated in fresh medium containing 1.0 mg/mL of mannose for a duration of 2 h at 37 °C, aiming to effectively block the mannose receptor (MR). Following this incubation period, we further cultured the cells for an additional 4 h, allowing for sufficient interaction between the nanovaccines and BMDCs. Subsequently, the cells were analyzed by detecting Cy5-mRNA fluorescence signals using flow cytometry.

To further visualize the intracellular uptake of nanovaccines, a laser scanning confocal microscope (LSCM) was employed. Following a 4-h incubation with the prepared nanovaccines, the BMDCs were gently washed with PBS and fixed with 4 % paraformaldehyde for 10 min. The nuclei were then stained with DAPI for 3 min, enhancing their visibility. Finally, the samples were observed under the LSCM (ZEISS LSM780, Germany), revealing the precise localization and distribution of the nanovaccines within the cells. To investigate the endosomal escape of mRNA, we incubated Cy5-mRNA, LNP/Cy5-mRNA, and TLNP/Cy5-mRNA in BMDCs cells for 6 h. Following this, the cells were labeled with Lyso-Tracker Green (supplied by Beyotime Biotech. Inc., Shanghai, China) for 15 min. Once cell fixation and nuclear staining were completed, the fluorescent images were observed and analyzed using LSCM.

To elucidate the cellular uptake mechanism of nanovaccines, we conducted a validation study on the endocytosis pathway in BMDCs. Briefly, BMDCs (5×10^4 cells per well in a 24-well plate) were pretreated with chlorpromazine (1 μg/mL, inhibiting clathrin-mediated endocytosis), amiloride hydrochloride (10 μg/mL, inhibiting micropinocytosis-mediated endocytosis), and methyl-β-cyclodextrin (10 mM, inhibiting lipid raft-mediated endocytosis) at 37 °C for 30 min prior to incubation with TLNP/Cy5-mRNA nanovaccines for 4 h. Furthermore, to ascertain the temperature-dependency of endocytosis, BMDCs were incubated with TLNP/Cy5-mRNA nanovaccines without inhibitors at 4 °C for 4 h. Following this, the cells were digested, centrifuged, washed with PBS, and analyzed using flow cytometry. The TLNP/Cy5-mRNA nanovaccines without inhibitors served as the positive control.

2.6. Gene transfection in BMDCs

The mRNA transfection experiments involved the utilization of two distinct messenger RNAs: mFluc encoding luciferase protein and mEGFP encoding the green fluorescent protein reporter gene. Briefly, BMDCs were plated in 6-well plates, achieving a density of 2.0×10^5 cells per well, and allowed to incubate overnight. Subsequently, mFluc loaded LNP, mFluc loaded TLNP, mEGFP loaded LNP, and mEGFP loaded TLNP were introduced into the wells and incubated overnight, maintaining a final mRNA concentration of 1 μg/mL. MAX was used as the positive control for mRNA transfection according to the manufacturer's protocol. For luciferase detection, the cells were lysed using 200 μL of cell lysate per well and stored at −80 °C for 1 h to ensure complete cell lysis. Following this, 25 μL of cell lysate was combined with 100 μL of luciferase substrate. The relative light units (RLUs) were then measured using a luminometer and normalized based on their corresponding protein content. The luciferase expression efficiency was determined by calculating RLU/mg. For EGFP detection, the transfected cells were initially observed under an inverted fluorescent microscope (TI-S, Nikon, Japan). Subsequently, the cells were collected, centrifuged at 1000 rpm for 3 min, and washed three times with cold PBS buffer.

Finally, the harvested cells were analyzed using a flow cytometer, and the data were processed through Flowjo software.

2.7. Immunomodulatory effect in BMDCs

The immunomodulatory effects of nanovaccines were assessed in BMDCs. Initially, BMDCs were seeded into 6-well plates, achieving a density of 2.0×10^5 cells per well. These cells were then incubated overnight to allow for optimal cell attachment and settling. Subsequently, PBS, mOVA loaded TLNP, cGAMP loaded TLNP, mOVA and cGAMP loaded LNP (NVs), mOVA and cGAMP loaded TLNP (TNVs), as well as the LPS positive control group, were introduced into the wells and co-incubated for 24 h. The final concentration of mRNA was maintained at 1 μg/mL. After the incubation period, both the BMDCs and the supernatant were collected for evaluation. The maturation state of the BMDCs induced by the nanovaccines was examined using specific markers, including anti-CD11c, anti-CD80, anti-CD86, and anti-MHCII antibodies. These markers provided insights into the activation status and phenotypic changes of the BMDCs. Additionally, the antigen cross-presentation ability of the BMDCs was assessed by measuring the percentage of SIINFEKL-H2k$^+$ cells within the CD11c$^+$ cell population using a flow cytometer. This analysis provided information on the efficiency of antigen presentation and the subsequent activation of T cells. The collected data were then analyzed using FlowJo software. Furthermore, the supernatant was evaluated for the secretion of cytokines, including interleukin-12p70 (IL-12p70), interleukin-6 (IL-6), tumor necrotic factor (TNF-α), and interferon-β (IFN-β) using ELISA kits. These cytokines play crucial roles in immune modulation and inflammatory responses, and their quantification provided valuable insights into the immunomodulatory potential of the nanovaccines.

The activation status of phosphorylated IRF3 (pIRF3), a crucial indicator of STING signal pathway, was assessed via Western blot analysis. To achieve this, the gathered BMDCs were first lysed using a RIPA lysis buffer. Following protein quantification with the BCA protein quantification kit and a brief boiling step for 10 min, the samples underwent SDS-PAGE electrophoresis (Bio-Rad, USA), with a loading quantity of 15 μg per sample. After transmembrane and serum blocking, the membranes were incubated overnight at 4 °C with rabbit anti-mouse primary antibodies targeting phosphor-IRF3 and β-actin. Subsequently, the membranes were washed five times with TBST solution and then incubated with HRP-conjugated goat anti-rabbit secondary antibody for 45 min at room temperature. Finally, the peroxidase activity was captured using an enhanced chemiluminescence (ECL) detection system, and the results were quantified with the Image J software.

To validate the activation of the STING signaling pathway, we employed a real-time quantitative polymerase chain reaction (RT-qPCR) assay to track the CXCL10 gene's expression. Initially, we extracted the total RNA from the activated BMDCs using RNA extraction kits from TIANGEN Biotech (Beijing) Co., Ltd. Following this, the isolated RNAs were accurately quantified, and 1 μg of each sample was subjected to reverse transcription using reagents from APExBIO Technology LLC, USA. Subsequently, we amplified and monitored the expression levels of the CXCL10 gene using a 2 × SYBR Green qPCR Master Mix (APExBIO Technology LLC, USA) in a PCR instrument from Applied Biosystems, USA. To ensure consistency and accuracy, GAPDH served as the housekeeping gene. The primers specific for CXCL10 and GAPDH were as follows: CXCL10-fwd 5′-GACGGTCCGCTGCAACTG-3′ and CXCL10-rev 5′-GCTTCCCTATGGCCCTCATT-3′ for CXCL10, while GAPDH-fwd 5′-GGGTGTGAACCACGAGAAATA-3′ and GAPDH-rev 5′-GTCATGAGCCCTTCCACAAT-3′ were used for GAPDH.

2.8. Construction of stable transfection of OVA-expressing lewis lung cancer cells (LLC-OVA)

A stable LLC-OVA expression cell line was successfully constructed via a lentiviral infection approach. In this procedure, 293T cells served

as host cells for lentiviral particle packaging, grown in Dulbecco's Modified Eagle Medium (DMEM) enriched with high glucose and 10 % fetal bovine serum. Initially, the 293T cells were seeded onto 6-well plates, maintaining a density of 2.0×10^5 cells per well, and incubated overnight. Subsequently, Lipofectamine™2000, pLVs-CMV-OVAL-3xFLAG-Puro, pSPAX2, and pMD2.G were combined in a weight ratio of 4:4:3:1 and allowed to complex for 10 min. These complexes were then added to the wells and incubated overnight, maintaining a final pMD2.G concentration of 0.25 μg/mL. Following a 6-h incubation, the supernatant was replaced with fresh medium and incubated for another 44 h. The resulting lentivirus particles were harvested and purified using a Universal Virus Concentration Kit.

After preparing the lentiviral supernatant, LLC cells were cultured in RPMI1640 medium enriched with high glucose and 10 % fetal bovine serum. These cells were then seeded onto 6-well plates, maintaining a density of 2.0×10^5 cells per well, and incubated overnight to ensure optimal growth conditions. Subsequently, the diluted lentiviral supernatant was gently added to each well in a volume ratio of 1:1, ensuring uniform distribution of the virus particles throughout the culture. The cells were incubated with the lentivirus for 24 h, after which the supernatant was replaced with fresh lentiviral supernatant. To maintain cell health and promote lentiviral infection, the cells were transferred to fresh medium containing puromycin (2 μg/mL) and the medium was replaced every 2–3 days. Following a week of cultivation, the LLC-OVA cells were successfully harvested, ready for further experimentation.

2.9. Gene transfection in vivo

The Balb/c mice (male, 8-week-old) were procured from Charles River Company (Beijing, China). The entire animal research was granted approval by the Animal Care and Use Committee of Jilin University, China, ensuring strict compliance with ethical standards. The nanovaccines, encapsulating mFluc, were administered intramuscularly into the gluteal muscle of the hind leg of the mice. The injection dose consisted of 50 μL containing an equivalent of 2 μg of mFluc. Twenty-four hours later, the luciferase substrate was administered intraperitoneally in a volume of 200 μL (3 mg/mouse). Following a 10-min interval, the expression of luciferase in the mice was observed and analyzed using a small animal in vivo imaging equipment (IVIS Lumina LT III, PE, USA).

2.10. Immunomodulatory effect in vivo

The C57BL/6 mice (male, 8-week-old) were sourced from Charles River Company in Beijing, China. The mice underwent intramuscular injections in their hind leg gluteal muscles with NVs, TNVs, as well as a PBS control. Each immunization dose consisted of 50 μL, with an mRNA equivalent of 2 μg per mouse. This immunization process was repeated a total of three times, with injections administered weekly. Seven days after the final immunization, the mice were euthanized, and their inguinal lymph nodes were excised and blood samples were collected. The lymph nodes were then digested and filtered, and a single-cell suspension was prepared. Flow cytometry was utilized to analyze DC cell maturation (CD11c$^+$MHCII$^+$ and CD11c$^+$CD80$^+$) and antigen cross-presentation (SIINFEKL-H2kb$^+$CD11c$^+$) within the lymph nodes. Additionally, ELISA technology was employed to detect immune-related factors in the serum, including IL-6, TNF-α, and IFN-γ, in accordance with the manufacturer's protocols.

2.11. Establishment of LLC-OVA tumor models

To establish a subcutaneous LLC-OVA tumor model in the dorsal region of mice, the mice (C57BL/6, male, 6-week-old) were anesthetized to ensure a comfortable sedation throughout the injection procedure. Subsequently, LLC-OVA cells were injected subcutaneously into the dorsal region of the mice using a sterile syringe, with a concentration of 1.0×10^6 cells suspended in 50 μL of PBS buffer. Tumor sizes were

monitored every alternate day using a caliper, and tumor volumes were calculated using the formula: V (mm^3) = 0.5 ab^2, where 'a' represented the longer diameter, and 'b' denoted the shorter diameter.

2.12. Therapeutic nanovaccine in the LLC-OVA model

After successfully establishing LLC-OVA tumor models on day 0, the mice exhibited tumor sizes of approximately 85 mm^3 on day 7. Subsequently, the mice with suitable tumor sizes were randomly assigned to three distinct groups, with five mice per group. These groups received intramuscular injections into the gluteal muscle of the hind leg with PBS, NVs, and TNVs, respectively. The immunization dose consisted of 50 μL, with an mRNA equivalent of 2 μg per mouse. A total of three injections were administered, with each injection separated by three days. From day 7 onward, the tumor sizes and body weights were monitored every two days. By day 19, the average tumor volume in the PBS group had reached approximately 1500 mm^3, prompting the euthanasia of mice from all groups to comply with the Animal Care and Use Committee regulations of Jilin University.

Subsequently, the inguinal lymph nodes and tumors were surgically excised and digested into a single-cell suspension. The cells from the lymph nodes were analyzed for DC cell maturation (CD11c$^+$MHCII$^+$ and CD11c$^+$CD80$^+$) using a flow cytometer. Furthermore, the quantification of various immune cells within the tumors was conducted, including CD8$^+$ T cells (CD3$^+$CD8$^+$), CD4$^+$ T cells (CD3$^+$CD4$^+$), and M1 cells (CD11b$^+$CD8$^+$F4/80$^+$).

Finally, the mean fluorescence intensity of PD-L1 expression on tumor cells was detected using a flow cytometer and analyzed via FlowJo software. These comprehensive assessments provided insights into the tumor growth, immune cell infiltration, and PD-L1 expression patterns within the tumor microenvironment.

2.13. Combination therapy of anti-PD-L1 and therapeutic nanovaccine in the LLC-OVA model

After successfully establishing LLC-OVA tumor models on day 0, the mice exhibited tumor sizes of approximately 80 mm^3 on day 7. At this point, mice with suitable tumor sizes were randomly divided into four distinct groups, with five mice in each group. These groups included PBS, anti-PD-L1, TNVs, and a combination of TNVs and anti-PD-L1. The TNVs were administered intramuscularly in a volume of 50 μL, containing 2 μg of mRNA per mouse, into the gluteal muscle of the hind leg. Meanwhile, the anti-PD-L1 antibody was injected intraperitoneally in a volume of 200 μL, at a concentration of 2.5 mg/kg body weight. Both treatments were administered three times, with intervals of three days between injections. From day 7 onward, the tumor sizes and body weights of the mice were closely monitored every two days. On day 19, when the average tumor volume in the PBS group exceeded 1500 mm^3, all mice were euthanized. Subsequently, the tumor tissues, spleens, and inguinal lymph nodes were surgically excised and digested into a single-cell suspension for immune cell analysis using flow cytometry. Blood samples were also collected for cytokine and biosafety analysis.

2.14. Combination therapy of anti-PD-L1 and prophylactic nanovaccine in the LLC-OVA model

C57BL/6 mice underwent TNVs treatments on day 0, followed by two booster vaccinations on day 7 and day 14. Each immunization dose consisted of 50 μL, containing 2 μg of mRNA per mouse. On day 21, LLC-OVA tumor cells were injected to induce the formation of subcutaneous tumors. Beginning on day 28, the mice received intraperitoneal injections of anti-PD-L1 antibody, administered in a volume of 200 μL and dosed at 2.5 mg/kg body weight. These injections were repeated three times, with a three-day interval between each administration. From day 28 onward, the tumor sizes were closely monitored every two days. Mice were euthanized when their tumor volume exceeded 1500 mm^3. The

tumor growth curve and the percentage survival rate for each group were analyzed using GraphPad Prism software.

2.15. Tumor re-challenge

On day 0, upon successfully establishing the 1st LLC-OVA tumor models, five mice exhibiting suitable tumor dimensions (around 85 mm^3) were chosen to undergo a combined therapeutic strategy. This strategy entailed intramuscular administrations of TNVs and intraperitoneal injections of anti-PD-L1 antibodies. The immunization dosage comprised 50 μL, equivalent to 2 μg of mRNA per mouse. This treatment protocol was administered three times, with each injection spaced three days apart. Following the completion of the final treatment session, the mice were subsequently rechallenged with LLC-OVA cells (1×10^6 cells/ 100 μL) in the contralateral dorsal region. The growth of the second tumors was subsequently monitored and measured for a duration of 39 days.

2.16. Long term toxicity

To ascertain the in vivo long-term toxicity of the targeted nanovaccines, they were intramuscularly administered into naïve mice on days 0, 7, and 14. The immunization dose comprised 50 μL, equivalent to 2 μg of mRNA per mouse. Following a 45-day period, blood samples were gathered for a comprehensive biochemical analysis, encompassing the enumeration of white blood cells (WBC), red blood cells (RBC), and platelets (PLT), as well as the assessment of alkaline phosphatase (AKP), aspartate aminotransferase (AST), alanine transaminase (ALT), uric acid (UA), blood urea nitrogen (BUN), and creatinine (CRE) levels.

2.17. Flow cytometry and western blot

In the combined therapy study involving anti-PD-L1 and therapeutic nanovaccines, the tumor tissues, lymph nodes, and spleens were digested, ground, and filtered through a 300-mesh strainer to yield single-cell suspensions. The cells were then fixed and stained with fluorescence-conjugated antibodies in a dark environment, adhering strictly to the manufacturer's protocols. These stained cells were analyzed using a flow cytometer (FCAS Celesta, BD, USA). The specific cell types examined in this study included: CD80$^+$MHCII$^+$CD11c$^+$ DC cells and SIINFEKL-H2kb$^+$CD11c$^+$ cells in the lymph nodes; CD3$^+$CD4$^+$ T cells, CD3$^+$CD8$^+$ T cells, CD11b$^+$CD80$^+$F4/80$^+$ M1 cells, CD3$^-$NK1.1$^+$ NK cells, CD4$^+$CD25$^+$FoxP3$^+$ Treg cells; and the mean fluorescence intensity of PD-L1 expression in the tumor tissues. Additionally, CD3$^+$CD4$^+$CD44$^+$CD62L^{low} T$_{EM}$ cells were analyzed in the spleens.

The PD-L1 expression was further assessed via Western blot analysis. To achieve this, the gathered tumor tissues were first cut into small pieces and lysed using a RIPA lysis buffer. Following protein quantification with the BCA protein quantification kit and a brief boiling step for 10 min, the samples underwent SDS-PAGE electrophoresis (Bio-Rad, USA), with a loading quantity of 15 μg per sample. After transmembrane and serum blocking, the membranes were incubated overnight at 4 °C with rabbit anti-mouse primary antibodies targeting PD-L1 and β-actin. Subsequently, the membranes were washed five times with TBST solution and then incubated with HRP-conjugated goat anti-rabbit secondary antibody for 45 min at room temperature. Finally, the peroxidase activity was captured using an enhanced chemiluminescence (ECL) detection system.

2.18. Histological and immunofluorescence analyses

The histological features of tumors and major organs, including the heart, liver, spleen, lung, and kidney, were meticulously stained with hematoxylin and eosin (H&E) in our study exploring the combination therapy of anti-PD-L1 and therapeutic nanovaccines. This staining procedure followed our previously established protocol [34]. The prepared slices were then examined through an upright microscope (DS-Ri2, Nikon, Japan), affording us detailed insights into the cellular structure and morphology.

For immunofluorescence staining, the tumor tissues were meticulously prepared into paraffin slices. These slices underwent a series of processing steps, including dewaxing paraffin, antigen retrieval, circle drawing, hydrogen peroxide blocking, serum blocking, primary antibody incubation, secondary antibody incubation, DAPI staining of cell nuclei, autofluorescence quenching, and mounting. This meticulous staining protocol ensures accurate and reliable results. The resulting slices were observed using a fluorescence microscope (Axio Imager A2, Zeiss, Germany), revealing crucial information about the cellular interactions and expression patterns.

The detailed protocols were provided as follows: For dewaxing paraffin, the sections were placed in xylene I for 15 min, followed by xylene II for another 15 min. They were then rinsed in anhydrous ethanol I for 5 min, anhydrous ethanol II for 5 min, 85 % alcohol for 5 min, and 75 % alcohol for 5 min. Finally, the sections were rinsed in distilled water. For antigen retrieval, the tumor slices were placed in a repair box filled with EDTA (pH 8.0) antigen repair solution and then subjected to antigen retrieval in a microwave oven. Ensure that the buffer does not evaporate excessively during this process, and prevent the slices from drying out. Once naturally cooled, immerse the slices in PBS (pH 7.4) and gently agitate them on a decolorizing shaker for three washes, each lasting 5 min. To draw circles and block hydrogen peroxide, gently blot the sections dry and use a histological pen to outline the tissue. Place the sections in a 3 % hydrogen peroxide solution, incubate in the dark at room temperature for 25 min to neutralize endogenous peroxidase, and then rinse in PBS (pH 7.4) using the decolorizing shaker for three washes of 5 min each. For serum blocking, apply BSA to the circled areas and incubate for 30 min. Subsequently, for primary antibody incubation, gently remove the blocking solution, add a mixture of PBS and the primary antibody to the sections at a specified ratio, and incubate the sections flat in a wet box at 4 °C overnight. To incubate the secondary antibody, rinse the slices in PBS (pH 7.4) on the decolorizing shaker for three washes of 5 min each. Then, slightly dry the sections and apply a fluorescent secondary antibody corresponding to the primary antibody, covering the tissue within the circle. Incubate in the dark at room temperature for 50 min. For DAPI staining, dry the sections slightly, apply DAPI staining solution (50 μg/mL) to the circled areas, and incubate in the dark at room temperature for 10 min. To quench autofluorescence, rinse the slices in PBS (pH 7.4) on the decolorizing shaker for three washes of 5 min each. Then, slightly dry the slices, apply autofluorescence quencher to the circled areas for 5 min, and rinse with running water for 10 min. Finally, for mounting, dry the sections slightly and affix them using an anti-fluorescence quencher mounting medium.

2.19. Enzyme linked immunosorbent assay (ELISA)

In the study of combined therapy utilizing anti-PD-L1 and therapeutic nanovaccine, the biomarkers present in the serum were quantified using ELISA. In brief, the serum samples were separated via centrifugation at 3000 rpm for 20 min. Subsequently, these samples were employed to detect interleukin-6 (IL-6), tumor necrosis factor alpha (TNF-α), interferon gamma (IFN-γ), AST, ALT, ALP, CRE, BUN, and UA levels.

2.20. Hematological evaluation

A thorough hematological analysis was conducted to assess the acute side effects and toxicities associated with various treatments. Specifically, within the context of the combined therapy utilizing anti-PD-L1 and therapeutic nanovaccine, the blood samples were meticulously analyzed, encompassing WBC count, RBC count, hemoglobin (HGB) levels, hematocrit (HCT) values, and PLT counts.

2.21. Statistical analysis

For the creation of graphs and comprehensive data analysis, the GraphPad Prism 8.0 software was utilized. Additionally, the FlowJo v10 software was employed for flow cytometry analysis. To determine statistical significance, the Student's t-test was applied.

3. Results and discussion

3.1. Preparation and characterization of mRNA-loaded targeted nanovaccines

The mRNA-loaded targeted lipid nanoparticles were meticulously formulated with SM-102, DSPC, Cholesterol, DMG-PEG2000, and DSPE-PEG2000-Mannose in molar ratios of 50:10:38.5:1.2:0.3. In contrast, the non-targeted LNP employed the traditional molar ratio of 50:10:38.5:1. To fashion tumor mRNA nanovaccines, we selected OVA-mRNA, which encodes ovalbumin as a model antigen. OVA serves as a specific antigen

for LLC-OVA cells, a Lewis lung cancer stable cell line expressing OVA protein. To augment the immunogenicity of these nanovaccines, we incorporated a cGAMP agonist. cGAMP agonists bind to and activate receptors on APCs, initiating a cascade of intracellular signaling events that stimulate various cellular responses and inflammatory cytokine production, vital for mounting an effective immune response [22]. Utilizing a microfluidic approach, the nanovaccines were meticulously prepared, maintaining an organic to aqueous phase volume ratio of 1:3 and flow rates of 4 mL/min and 12 mL/min, respectively (Fig. 1A). Clinically, the nanovaccine particle size is crucial for efficacy and safety. Ideal nanovaccines should strike a balance between being small enough for efficient immune cell delivery and uptake, yet large enough to evade rapid clearance by the body's natural defense mechanisms [35].

As depicted in Fig. 1B and C, the NVs and TNVs exhibited a homogenous distribution of particle sizes ranging from 80 to 85 nm (PDI: 0.05 to 0.09). The TEM image in Fig. 1C confirmed the spherical shape in morphology and uniform dispersion of the targeted nanovaccines. Additionally, the SEM image further verified its spherical structure and
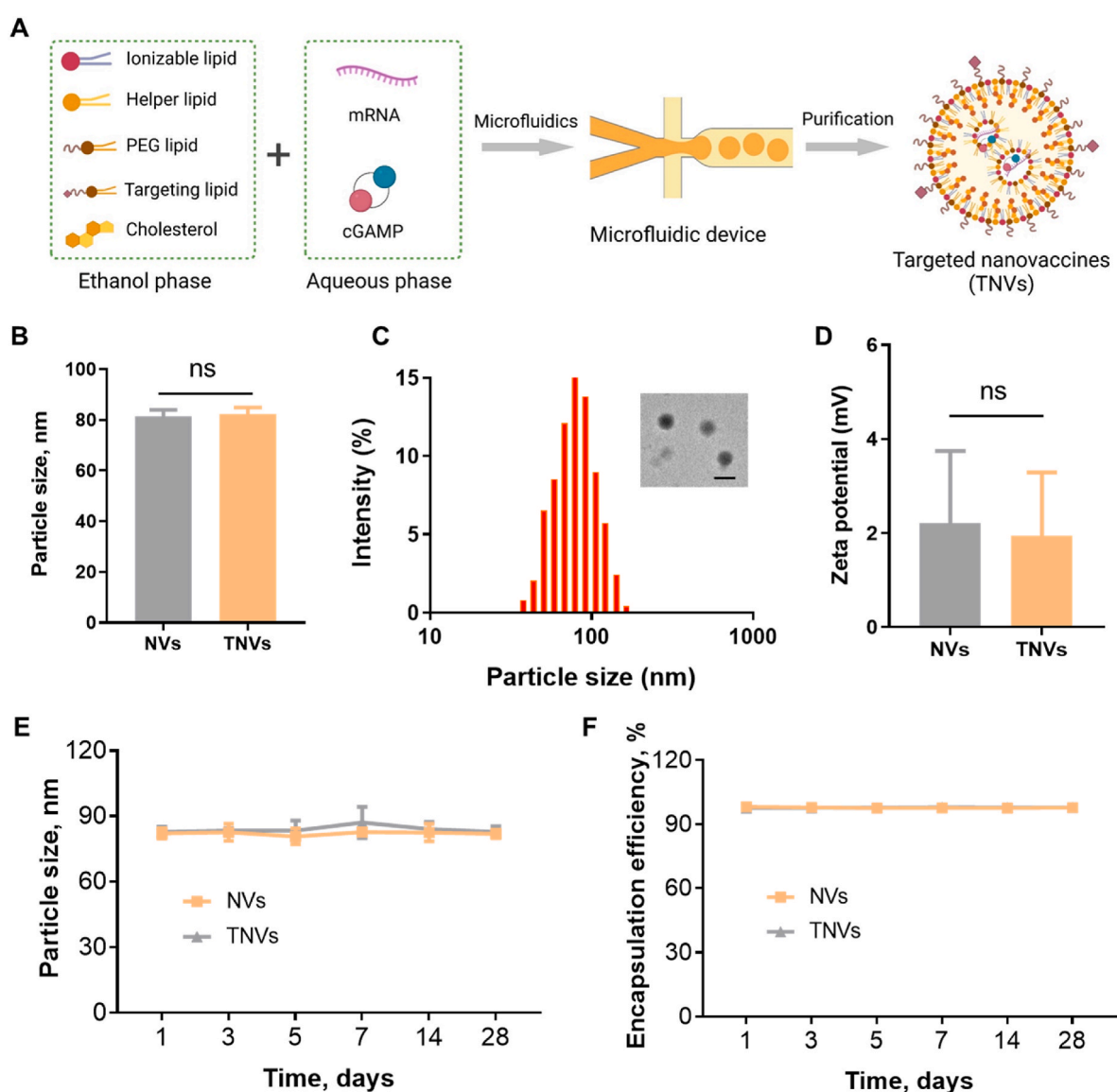

Fig. 1. Preparation, characterization and stability studies of mRNA-loaded targeted nanovaccines (TNVs). (A) Schematic representation of the composition and preparation pathway for targeted nanovaccines (TNVs). (B) Detailed analysis of the particle size distribution for NVs and TNVs. (C) Particle size distribution profiles of TNVs, along with TEM images revealing the surface morphology of TNVs. Scale bar = 100 nm. (D) Zeta potential measurements for NVs and TNVs. (E) Temporal changes in particle size for NVs and TNVs over a 28-day incubation period at 4 °C. (F) Changes in mRNA encapsulation efficiency for NVs and TNVs over a 28-day incubation period at 4 °C. This analysis highlights the stability and mRNA retention capacity of the nanovaccines over time. ns = not significant.

size (Fig. S1). Notably, nanovaccines with a particle size ranging from 50 to 200 nm are generally preferred due to their increased likelihood of internalization by APCs, triggering the desired immune response. Conversely, nanovaccines exceeding 200 nm may be rapidly cleared by the reticuloendothelial system (RES), compromising their bioavailability and efficacy. On the other hand, particles smaller than 50 nm may not be effectively internalized by APCs, limiting their immunogenicity [36]. Therefore, it is imperative to carefully consider the suitable particle size during the development of clinically effective nanovaccines. The nanovaccines exhibited near-neutral surface charges ranging from 0.76 to 3.84 mV, primarily attributed to the presence of the neutral ionizable lipid SM102 (Fig. 1D). These physical characteristics of NVs and TNVs are summarized in Table 1. Furthermore, the stability of the nanovaccines was evaluated by incubating them under 4 °C for different time points (0 d, 1 d, 3 d, 5 d, 7 d, 14 d, and 28 d). The particle sizes and drug encapsulation efficiencies (EE%) of NV and TNVs were determined at these time points. As shown in Fig. 1E and F, the particle size and mRNA encapsulation rate of the nanovaccines remained stable for four weeks when stored at 4 °C, confirming their stability.

3.2. Biological functional evaluation of nanovaccines in BMDCs

The importance of cellular toxicity in nanovaccines lies in its profound influence on vaccine potency and human wellbeing. These nanoscale delivery vehicles, thanks to their unique properties, offer remarkable advantages in efficiently targeting antigens to immune cells, stimulating robust immune responses. However, if these nanoparticles exhibit cytotoxicity, they can potentially cause cellular damage, disrupt normal immune function, and compromise the vaccine's ability to elicit protective immunity. Cellular toxicity can lead to a range of adverse effects, including immune cell death, inflammatory responses, and the development of autoimmune diseases. Such toxicities can not only reduce the immunogenicity of nanovaccines but also pose a safety risk to recipients [37]. Therefore, we prioritized the evaluation of the cytotoxicity of the prepared nanovaccines in BMDCs. Our results demonstrated that both NVs and TNVs exhibited minimal toxicity under the experimental conditions, indicating their excellent biocompatibility (Fig. 2A). This finding is crucial in ensuring the safety and efficacy of nanovaccines, paving the way for their potential use in clinical settings.

The crucial factor for the successful preparation of mRNA nanovaccines lies in their high expression efficiency. To assess the gene expression efficacy of the nanovaccines, we conducted an in vitro transfection study in BMDCs using EGFP-mRNA and Fluc-mRNA. The results, presented in Fig. 2B and C, demonstrate that both nanovaccines exhibited remarkable transfection efficiency in BMDCs, evident from the robust expression of green fluorescent protein. Quantitative flow cytometry further revealed that targeted nanovaccines exhibited superior protein expression efficiency compared to non-targeted nanovaccines. MAX group demonstrated the highest transfection efficiency, while the difference was not statistically significant when compared to the targeted nanovaccine TNVs group (Fig. S2). This conclusion was further reinforced by the luciferase quantitative experiment (Fig. S3), attributed primarily to the introduction of APCs-targeted segments. These findings underscore the potential of mRNA nanovaccines in eliciting robust immune responses and their promise in clinical applications.

Mannose Receptor (MR), a pivotal player in the innate immune system, serves as both a pattern recognition receptor and an endocytic receptor. Predominantly expressed on the cell membrane of macrophages and dendritic cells, the MR boasts multiple extracellular domains

that are adept at recognizing and binding a diverse array of endogenous and exogenous ligands. Notably, it possesses the capability to bind carbohydrate structures, including fucose and mannose [38]. As depicted in Fig. S4, BMDCs exhibited conspicuously high levels of MR protein on their cellular surface compared with that of LLC-OVA cells.

Subsequently, we delved into the APC-targeting capabilities of the nanovaccines. The APC-targeted mRNA nanovaccines serve a crucial role in delivering mRNA encoding antigens directly to APCs, primarily dendritic cells, with the aim of eliciting specific immune responses. These nanovaccines harness the power of mRNA technology, encoding antigens within a nanoparticle delivery system, enabling precise and controlled antigen expression within the APCs. Initially, we assessed the impact of incorporating targeted molecule DSPE-PEG2000-Mannose in TNVs at varying molar ratios on the endocytosis efficiency in BMDCs. With the increased proportion of DSPE-PEG2000-Mannose, the endocytosis efficiency was notably enhanced. Intriguingly, when the ratios reached 0.3:1.2, 0.4:1.1, and 0.5:1.0, there was no significant variation in the transfection efficiency (Fig. S5). Considering economic costs and practicability, our study ultimately opted for a ratio of 0.3:1.2 for further investigation. As depicted in Fig. 2D, the TNVs/Cy5-mRNA group exhibited the highest mRNA endocytosis efficiency compared to the non-targeted group and the free Cy5-mRNA group. Furthermore, the results from LSCM provided qualitative evidence of the enhanced endocytosis of targeted nanovaccines (Fig. 2E). Next, we validated the targeted endocytosis mechanism of the nanovaccines through a mannose competition experiment. The findings revealed that BMDCs targeted with TNVs exhibited a marked increase in Cy5-mRNA endocytosis compared to non-targeted NVs. Notably, when mannose was utilized to impede the MR-mediated endocytosis, the endocytosis efficiency of Cy5-mRNA in the targeted TNVs group was significantly reduced, whereas the non-targeted NVs group exhibited no substantial changes (Fig. S6). These results further confirm the specificity of mannose moiety binding to dendritic cells.

To elucidate the intracellular uptake mechanism of nanovaccines, we conducted a validation study on the endocytosis pathway in BMDCs. As depicted in Fig. S7, the uptake efficiency of TLNP/Cy5-mRNA nanovaccines at 4 °C was significantly lower compared to that at 37 °C, suggesting an energy-dependent cellular uptake process. Additionally, pre-incubation with methyl-β-cyclodextrin and amiloride hydrochloride reduced the cellular uptake efficiencies of TLNP/Cy5-mRNA nanovaccines to 49.1 % and 51.8 %, respectively. In contrast, chlorpromazine only achieved a moderate reduction of approximately 14.9 % in cellular uptake. These findings indicate that micropinocytosis- and lipid raft-mediated endocytosis play a more crucial role than clathrin-mediated endocytosis in facilitating the transmembrane transport of TLNP/Cy5-mRNA nanovaccines by BMDCs, ultimately resulting in high delivery efficiency.

By specifically targeting BMDCs, mRNA nanovaccines aim to maximize the immunogenicity of the encoded antigens. Once the mRNA nanovaccines successfully penetrates into BMDC cells, both the NVs and TNVs groups exhibited favorable endosome escape efficiencies of mRNA, which is crucial for the successful implementation of tumor cell immunotherapy (Fig. S8). This ultimately benefits a remarkably efficient expression of antigens, which are then presented on the cell surface to activate T-cells and initiate adaptive immune responses. The targeted delivery ensures efficient antigen presentation to the immune system, leading to stronger and more specific immune responses.

3.3. The immunomodulatory impact of nanovaccines in BMDCs

Upon internalization by APCs, mRNA is translated into antigens, which undergo processing and are subsequently presented on the cell surface alongside Major Histocompatibility Complex (MHC) molecules. Concurrently, activated APCs secrete cytokines that initiate subsequent T cell immune responses. In this study, nanovaccines were pre-loaded with mOVA and cGAMP agonists. Following a 24-h incubation with

Table 1
Physical characteristics of nanovaccines.

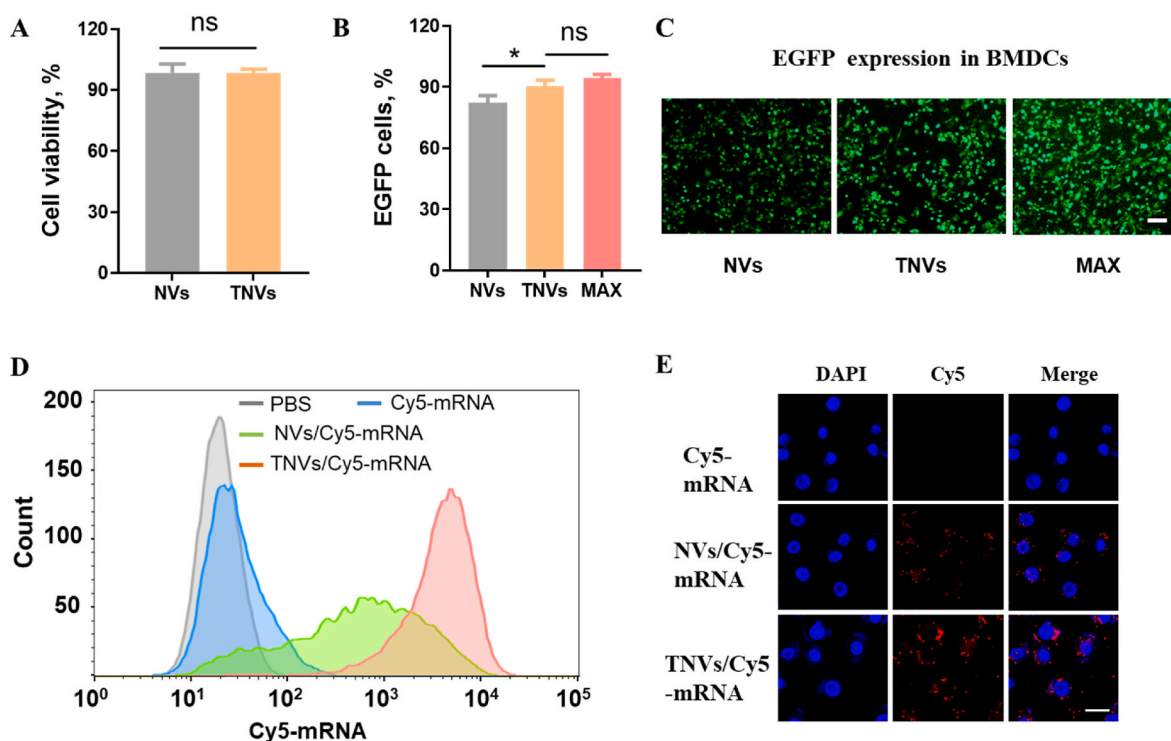|	EE (%)	Zeta potential (mV)	Size (nm)	PDI
NVs	98.17 ± 0.57	2.22 ± 1.62	81.33 ± 2.91	0.066 ± 0.011
TNVs	97.50 ± 1.01	1.94 ± 1.18	82.20 ± 3.02	0.079 ± 0.012

Fig. 2. Evaluation of the biological functionality of nanovaccines in BMDCs. (A) Examination of the cytotoxic effects of nanovaccines on BMDC cells. (B) Quantitative assessment of EGFP expression in BMDCs through flow cytometry. The commercial transfection reagent MAX was used as a positive control. (C) Qualitative analysis of EGFP expression in BMDCs. The commercial transfection reagent MAX was used as a positive control. Scale bar = 100 μm. (D) Evaluation of nanovaccine endocytosis in BMDCs through flow cytometry, utilizing Cy5 mRNA as a fluorescent marker. (E) Visualization of intracellular uptake of nanovaccines in BMDCs by LCSM. Scale bar = 10 μm *p < 0.05, ns = not significant.

BMDCs, we examined BMDC cell maturation, antigen cross-presentation, and cytokine secretion (Fig. 3A). We first validated the immune activation of mOVA and cGAMP loaded targeted lipid nanoparticles in BMDCs. As shown in Figs. S9A and B, TLNP-cGAMP and TLNP-mOVA/cGAMP groups displayed a significantly higher level of BMDC maturation ratio compared with that of TLNP-mOVA group, indicating the crucial role of the cGAMP adjuvant molecule in the activation of BMDCs. While in antigen cross-presentation assay, TLNP-mOVA and TLNP-mOVA/cGAMP groups effectively bolstered the antigen cross-presentation effect of BMDCs. Specifically, the inclusion of the cGAMP adjuvant molecule further amplified this effect. Conversely, the groups devoid of mOVA failed to demonstrate any notable antigen cross-presentation effect (Fig. S9C). Based on these findings, we incorporate the combination of mOVA and cGAMP in the subsequent studies to integrate their respective advantages. As depicted in Fig. 3B and C, all experimental groups demonstrated significantly improved BMDC cell maturation rates compared to the PBS group. Notably, the TNVs group elicited a more robust stimulation of BMDC cell maturation than the NVs group, which was comparable to the LPS positive control group.

Generally, mRNA nanovaccines could activate immune responses at the cellular level by delivering mRNA to APCs and expressing antigen for cross-presentation. This leads to the activation of both helper and cytotoxic T-cells, triggering a coordinated immune response against the encoded antigens and providing protection against cancers [39,40]. Building on this understanding, we further investigated antigen cross-presentation. As shown in Fig. 3D, no antigen cross-presentation was observed in the LPS group or the PBS group. However, both nanovaccine groups exhibited significant antigen cross-presentation effects, with the targeted vaccine group achieving a notably higher antigen cross-presentation effect.

After the activation of APCs by vaccines, cytokines play a crucial role in immune activation. They orchestrate and harmonize the immune response by igniting and attracting diverse immune cell types, boosting

the production of effector molecules, and amplifying the immune system's subsequent anti-tumor actions [6]. Our study focused on the representative cytokines: IL-12p70, TNF-α, IL-6, and IFN-β. Fig. 3E, F, 3G and Fig. S10 clearly show that, in contrast to the NVs group, the secretion of these three cytokines in the TNVs group has significantly escalated, hinting at its promising clinical potential. Furthermore, the marked elevation in the secretion of INF-β (Fig. 3G) and the significant surge in CXCL10 mRNA levels (Fig. 3H) unequivocally demonstrate the activation of the STING pathway in BMDCs cells by cGAMP agonists. Additionally, nanovaccine treatment led to a notable enhancement in the expression of the downstream pIRF3 protein of the STING pathway, particularly in the targeted nanovaccine TNVs group, as evident from Fig. 3I–J. The activation of the STING pathway in APCs is pivotal for anti-tumor immunotherapy. It prompts the secretion of cytokines that directly target and eliminate tumor cells, primes the immune system for a more robust anti-tumor response, and recruits and activates other immune cells to combat tumor growth [41].

3.4. Immunomodulatory effect of nanovaccines in vivo

The immunomodulatory impact of nanovaccines is profound, particularly when it comes to their immune activation effects on tumor cells. Upon intramuscular injection, these nanovaccines are recognized and processed by APCs, subsequently presented to T cells. This interaction triggers a cascade of anti-tumor immune responses, effectively targeting and destroying tumor cells. In this study, we delved into the immunomodulatory potential of nanovaccines in vivo. Healthy mice received intramuscular injections of NVs, TNVs, or a PBS control three times, targeting the glute muscle of the hind leg. Seven days after the final immunization, the mice were euthanized, and inguinal lymph nodes were extracted along with blood samples for immunomodulatory analysis (Fig. 4A). As Fig. 4B and C demonstrate, the nanovaccine groups exhibited significantly improved maturation rates of DCs compared to
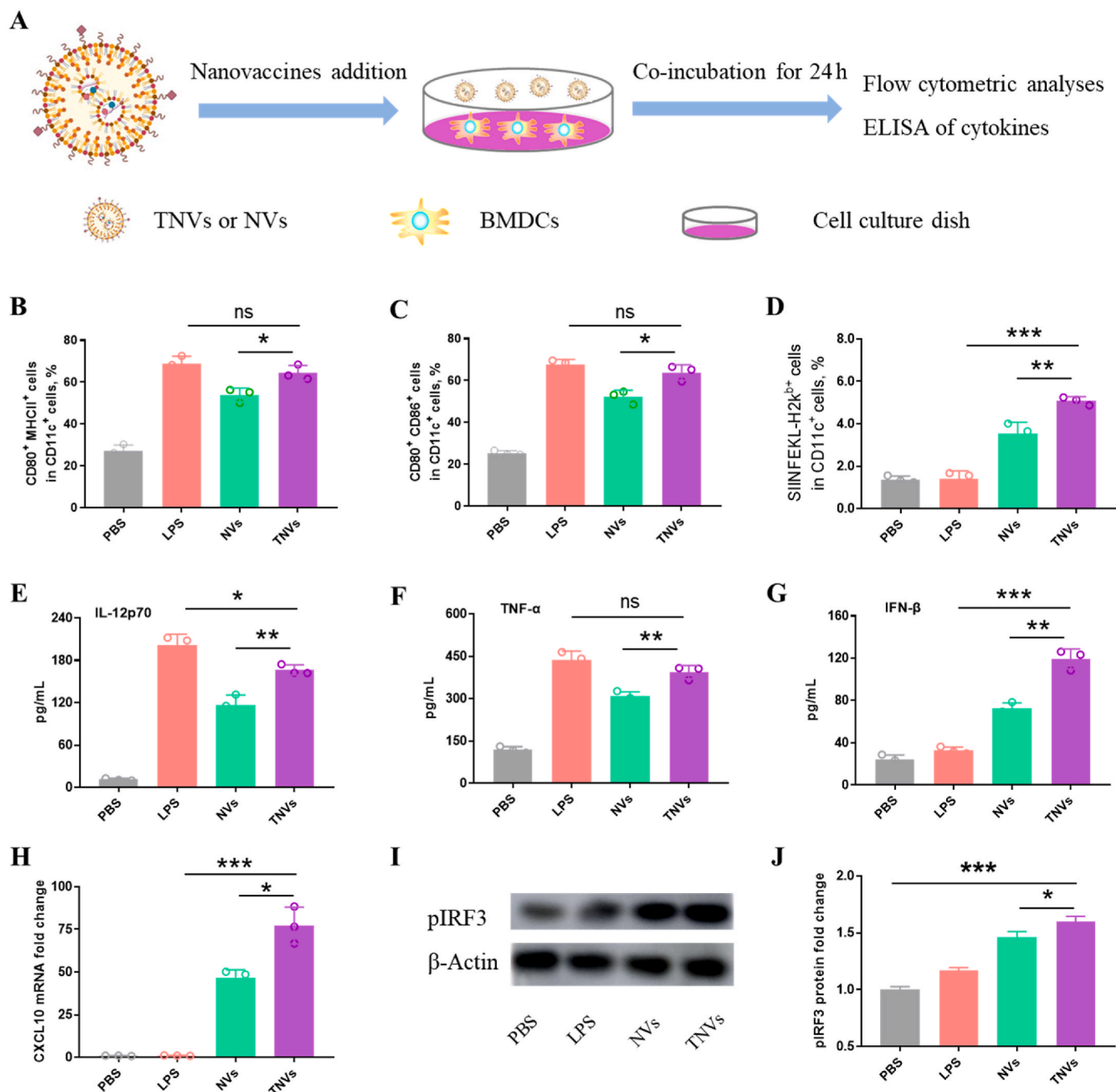
Fig. 3. The immunomodulatory impact of the targeted nanovaccines in BMDCs. (A) A schematic representation illustrates the immune activation process within BMDCs triggered by these targeted nanovaccines. (B–C) Monitoring of BMDC maturation follows the administration of nanovaccines. (D) The nanovaccines effectively induce antigen cross-presentation. (E–G) A comprehensive analysis of cytokine secretion by BMDCs after nanovaccine induction reveals a robust immune response. (H) CXCL10 mRNA expression in BMDCs by RT-qPCR after different treatments. (I) Detection of pIRF3 protein expression in BMDCs after nanovaccine treatment by western blot. (J) Quantitative analysis the pIRF3 protein expression in (I). *$p < 0.05$, **$p < 0.01$, ***$p < 0.001$, ns = not significant.

the PBS group. Notably, the TNVs group displayed an even more pronounced stimulatory effect on DC maturation than the NVs group. Furthermore, the TNVs group achieved a remarkable antigen-cross-presentation effect, indicating a stronger anti-tumor T cell immune response (Fig. 4D). Additionally, the secretion of cytokines in the TNVs group was significantly elevated compared to the NVs group (Fig. 4E and F and Fig. S11). This robust immunological activation was primarily attributed to the high expression of mRNA nanovaccine antigens. To validate this, we utilized Fluc-mRNA to assess antigen expression in mice. Bioluminescence was detected 24 h after intramuscular injection

of Fluc-mRNA-loaded NVs and TNVs. As shown in Fig. 4G, the luciferase expression efficiency in the TNVs group at the injection site was significantly increased compared to the NVs group. In contrast, the PBS control group exhibited no bioluminescence, providing further confidence for the follow-up investigation of the immune response elicited by nanovaccines in vivo. These encouraging results suggest that the meticulously prepared targeted nanovaccines possess promising potential as an anti-tumor therapeutic approach.
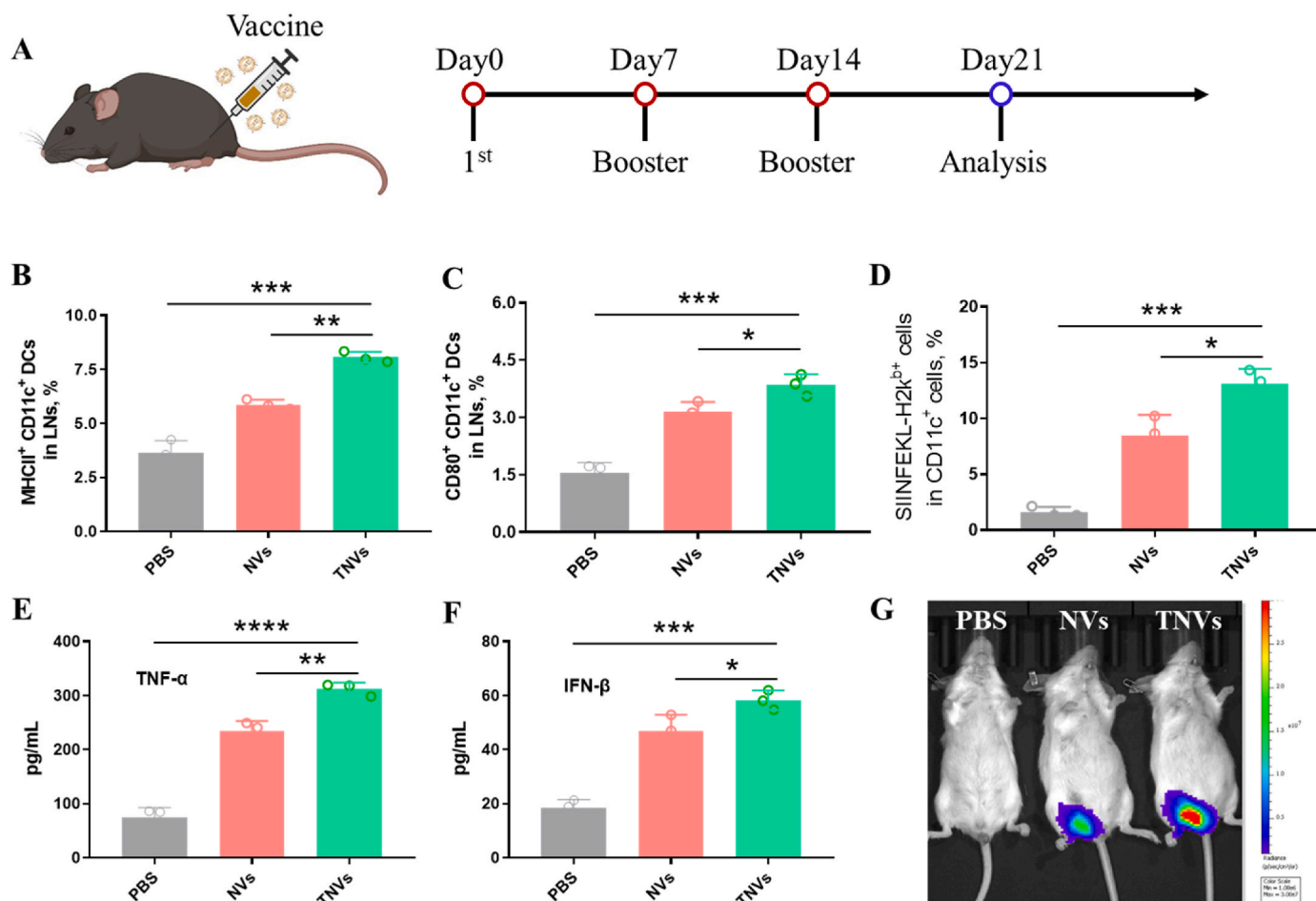
Fig. 4. The immunomodulatory capabilities of the targeted nanovaccines in vivo. (A) Illustrated is the activation of the immune system within the body, triggered by these precisely targeted nanovaccines. (B–C) Detection of the maturation process of DCs following the induction of nanovaccines in LNs is demonstrated. (D) The antigen cross-presentation stimulated by the nanovaccines within the LNs is highlighted. (E–F) The secretion of cytokines in the serum is detected after a 24-h intramuscular injection of the nanovaccines. (G) The expression of luciferase within the body is observed after a 24-h intramuscular injection of the nano-vaccines. *p < 0.05, **p < 0.01, ***p < 0.001, ****p < 0.0001.

3.5. Therapeutic nanovaccines

To evaluate the antitumor therapeutic efficacy of nanovaccines, we first generated LLC-OVA cells via lentiviral transduction. OVA, a tumor model antigen widely used in immunological studies, was chosen due to its immunogenicity and stability. The stable transfection of OVA into cell lines offered a valuable tool for studying tumor-specific immune responses. In this study, we established a subcutaneous LLC-OVA tumor model in the dorsal region of mice. Subsequently, the mice were intramuscularly immunized with nanovaccines three times (Fig. 5A). Tumor sizes and weights were monitored throughout the immunotherapy period. The mice were euthanized on the sixth day following the final immunization, adhering to animal ethical requirements, and the mechanisms underlying tumor immunity were analyzed. Tumor inhibition curves revealed that the TNVs group effectively inhibited tumor growth compared to other groups (Fig. 5B). As shown in Fig. 5C and D, compared to the PBS group, the maturation rates of DCs in inguinal LNs were significantly enhanced in the nanovaccine groups, with the TNVs group demonstrating superior stimulation of DC maturation compared to the NVs group. Furthermore, in tumor tissues, the proportions of CD4+ T cells (Fig. S12), CD8+ T cells (Fig. 5E), and M1 macrophages (Fig. 5F) were significantly improved by the TNVs group, indicating a stronger antitumor immune response. Notably, there was no significant difference in mouse weight among the groups during the entire antitumor treatment period, initially validating the safety of the

nanovaccines (Fig. S13). Despite the promising initial results, a trend towards rapid tumor growth emerged in the later stages of the therapeutic TNVs group. Prompted by this observation, we delved deeper into the expression of the PD-L1 immune checkpoint within the tumor tissues. Alas, we discovered a marked increase in PD-L1 protein expression among tumor cells across both nanovaccine treatment arms, leading to an augmented immune tolerance by the tumor cells. This revelation offers a plausible explanation for the limited effectiveness of nanovaccine treatment. Consequently, in our subsequent research, we elected to explore the combined therapeutic potential of tumor nanovaccines and immune checkpoint blockade.

3.6. Combination of nanovaccines with anti-PD-L1 antibody

Previously, anti-tumor vaccine studies revealed an increase in PD-L1 expression within tumor tissue following treatment. Leveraging this observation, the present investigation explored a combined therapeutic approach utilizing nanovaccines and anti-PD-L1 antibodies. The role of anti-PD-L1 antibodies lies in interrupting the inhibitory signaling cascade triggered by the interaction between PD-L1 and its cognate receptor PD-1 on T-cells. This blockade effectively restores the immune system's capacity to recognize and target tumor cells [42,43]. We then delved into evaluating the synergistic antitumor effects of combining therapeutic nanovaccines with anti-PD-L1 antibodies (Fig. 6A). Tumor growth was meticulously monitored every two days (Fig. 6B–F).
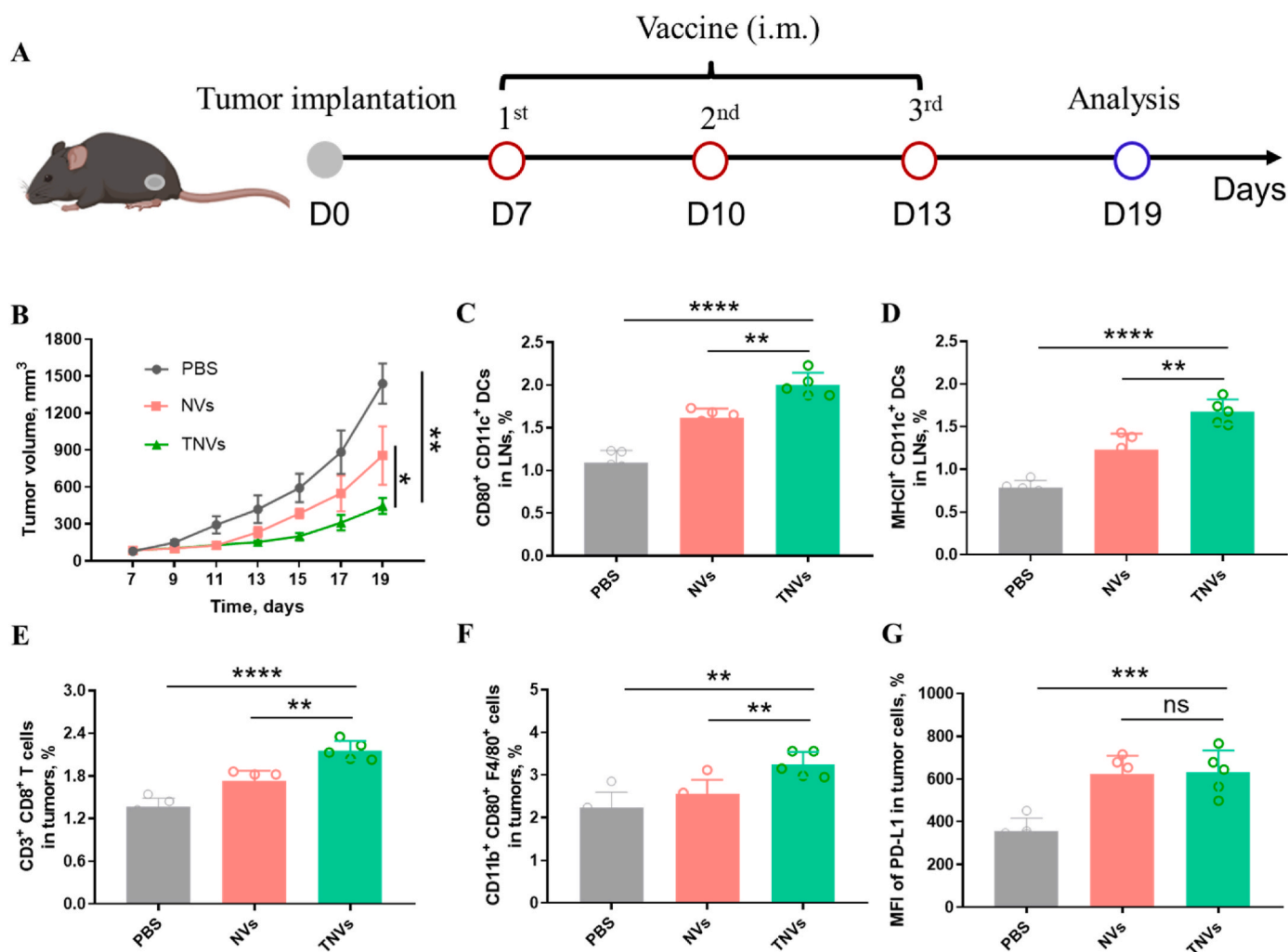
Fig. 5. Anti-tumor strategy by therapeutic nanovaccines. (A) Schematic diagram of anti-tumor strategy by therapeutic nanovaccines in LLC-OVA tumor model. (B) Tumor growth curves. (C–D) Maturation rates of DCs cells in inguinal LNs. The proportion of (E) CD8$^+$ T cells and (E) M1 macrophages in tumor tissues. (G) The mean fluorescence intensity of PD-L1 expressed in tumor cells. *$p < 0.05$, **$p < 0.01$, ***$p < 0.001$, ****$p < 0.0001$, ns = not significant.

Notably, monotherapy alone did not yield the desired antitumor effects (Fig. 6C and D), whereas the combined treatment demonstrated robust inhibition of tumor growth (Fig. 6E). This enhanced therapeutic effect is attributed to the synergistic immune stimulatory properties of both nanovaccines and anti-PD-L1 antibodies. To further validate our findings, we compared tumor weights across all treatment groups, confirming the superior antitumor effect of the combined therapy (Fig. S14). Histological analysis through H&E staining of tumor tissues revealed that the tumor tissue architecture in the TNVs + anti-PD-L1 combination therapy group exhibited profound alterations when contrasted with the control group and various single-therapy cohorts. These changes encompassed a marked expansion in the necrotic regions, a substantial reduction in tumor cell density, and a notable lightning of the chromatin, all of which underscored the effectiveness and success of the implemented treatment strategy (Fig. 6G). We further assessed the anticancer efficacy of prophylactic tumor TNVs combined with anti-PD-L1 antibody in the LLC-OVA tumor model. The therapeutic schema was illustrated in Fig. S15. The mice underwent three immunizations with TNVs, administered weekly. Subsequently, seven days after the final immunization, LLC-OVA cells were inoculated subcutaneously in the backs of the mice. Starting from day 28, anti-PD-L1 antibodies were administered intraperitoneally every four days, totaling three administrations. The tumor size and survival curves of the mice were closely monitored throughout the therapeutic process. The findings were analogous to those observed with therapeutic vaccines, wherein both monotherapy strategies fell short of achieving satisfactory results (Fig. S16). However, the combined regimen of TNVs and anti-PD-L1 induced optimistic antitumor responses, resulting in a prolonged survival time for the mice (Fig. S17). This observation provides additional evidence of the synergistic antitumor efficacy of this combined therapeutic strategy.

It is widely acknowledged that a crucial aspect of tumor immunotherapy lies in its immunological memory responses against rechallenged tumors. To validate the efficacy of our combined strategy in preventing tumor recurrence, we established an animal model for tumor re-challenge while administering the combined therapy. As depicted in Fig. S18, after the first tumor was treated with the combined therapy, secondary LLC-OVA tumors were inoculated into the contralateral flank. Mice that were immunized with PBS without prior tumor inoculation and inoculated with the same number of tumor cells served as the control group. Subsequently, the secondary tumors were monitored, and mice were deemed deceased when the tumor volume surpassed 1500 mm^3. Remarkably, the growth of secondary tumors in the combined therapy group was significantly suppressed, with all mice surviving and even 20 % failing to develop tumors. In contrast, all tumors in the PBS group grew and exceeded 1500 mm^3 within 25 days, highlighting the exceptional immunological memory protection offered by our designed combined strategy.
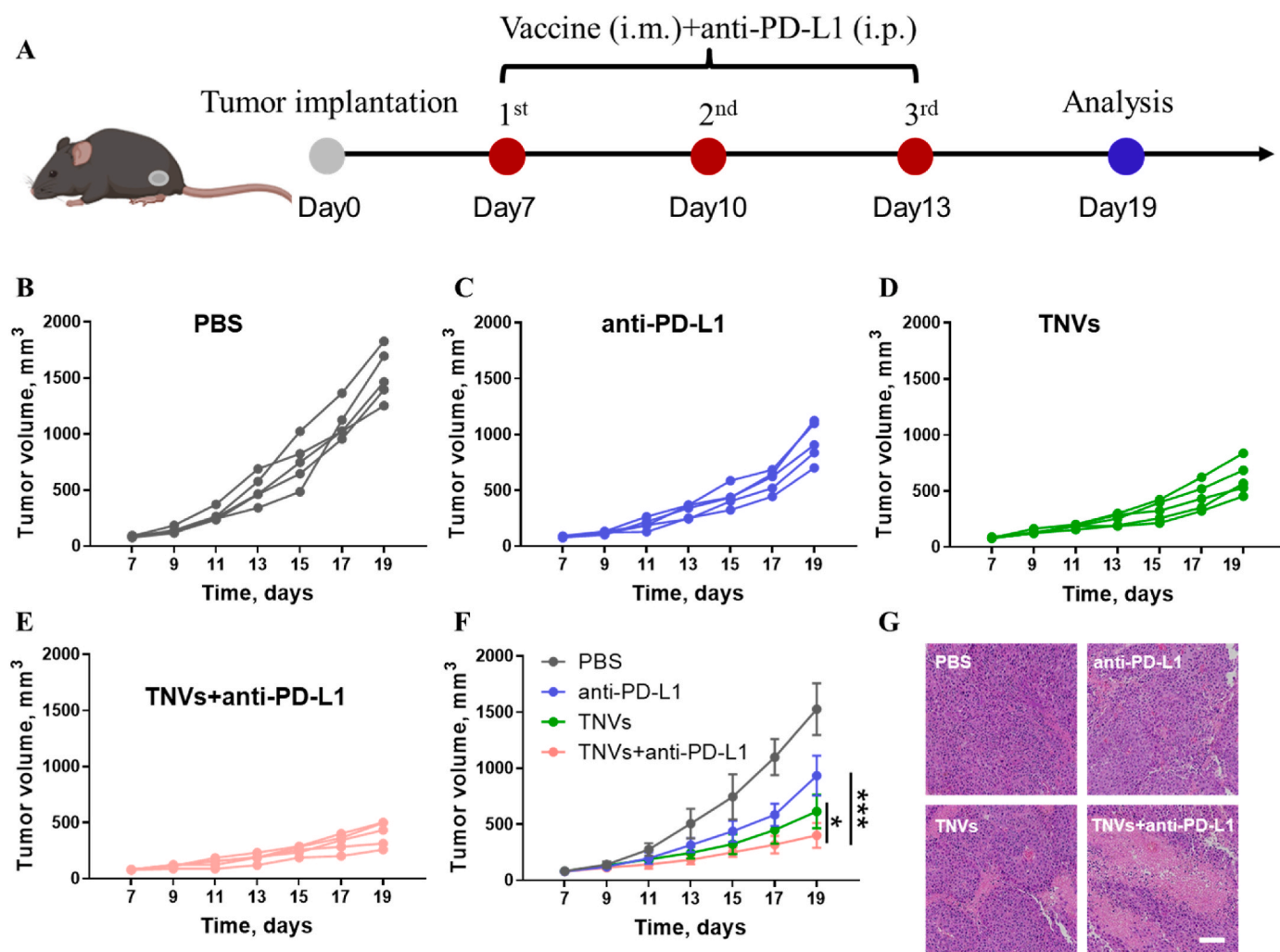
Fig. 6. Combination treatment utilizing therapeutic TNVs with anti-PD-L1 antibody. (A) Anti-tumor approach through the concurrent use of therapeutic TNVs and anti-PD-L1 antibody in the LLC-OVA tumor model. Antitumor approach through the growth patterns of tumors in the following treatment groups: PBS (B), anti-PD-L1 (C), TNVs (D), TNVs + anti-PD-L1 (E), and an overview of all treatment groups (F). (G) Histological analysis of tumor tissues through H&E staining, scale bar = 200 nm *$p < 0.05$, ***$p < 0.001$.

3.7. Mechanism of anti-tumor treatment

The mechanism of anti-tumor treatment encompasses multiple crucial components, including the maturation of dendritic cells (DCs) within the lymph nodes, diverse immune cell subsets within the tumor microenvironment, cytokines circulating in the bloodstream, and the utilization of immunofluorescence to assess tumor immunology [23]. DCs play a pivotal role in the immune system, serving as messengers between the immune system and other cellular components [44,45]. In the lymph nodes, DCs capture antigens, migrate towards T-cell zones, and present these antigens to T cells, thereby initiating an adaptive immune response against tumors. Both the TNVs and TNVs + anti-PD-L1 groups exhibited an elevated ratio of CD80+MHC II+ mature DCs in the inguinal lymph nodes (Fig. 7A), with the combined treatment group demonstrating an even higher proportion of mature DCs. Furthermore, both groups facilitated significant antigen cross-presentation, with no noteworthy differences observed between them (Fig. 7B).

Tumors encompass a diverse array of cell types, including tumor cells, immune cells, and various others. The intricate interplay between these cells shapes the immune response within the tumor microenvironment. For instance, tumor-associated macrophages (TAMs) and regulatory T lymphocytes (Tregs) can suppress the immune response, while tumor-infiltrating lymphocytes (TILs) and natural killer cells (NK

cells) can mediate anti-tumor immunity. Therefore, we analyzed CD4+ T cells (Fig. 7C), CD8+ T cells (Fig. 7D), M1 macrophages (Fig. 7E), NK cells (Fig. 7F), and Tregs (Fig. 7G) in tumor tissues. The results were intriguing: compared to the single treatment group, the combined treatment of TNVs and anti-PD-L1 effectively activated and augmented the proportion of anti-tumor immune cells, while concurrently reducing the proportion of immunosuppressive Tregs. Furthermore, a remarkable finding emerged: following treatment with the anti-PD-L1 antibody, the expression of PD-L1 protein on the surface of tumor tissue cells was significantly diminished (depicted in Fig. 7H). This observation indicates a synergistic anti-tumor therapeutic effect between the nanovaccine and anti-PD-L1 antibody. The immune memory effect induced by vaccines is pivotal for long-term anti-tumor protection. Once the initial immune response resolves, a population of memory T cells persists. These primed memory T cells are poised to respond promptly upon re-exposure to the same antigen. As demonstrated in Fig. 7I, the combination treatment group exhibited the most robust immune memory effect, which is more conducive to the body's ability to rapidly recognize and eliminate both primary and metastatic tumors, thereby inhibiting tumor metastasis and recurrence.

Cytokines, small proteins secreted by immune cells, play a pivotal role in regulating the immune response [46]. In the present study, we focused on the detection of cytokine secretion in serum samples.
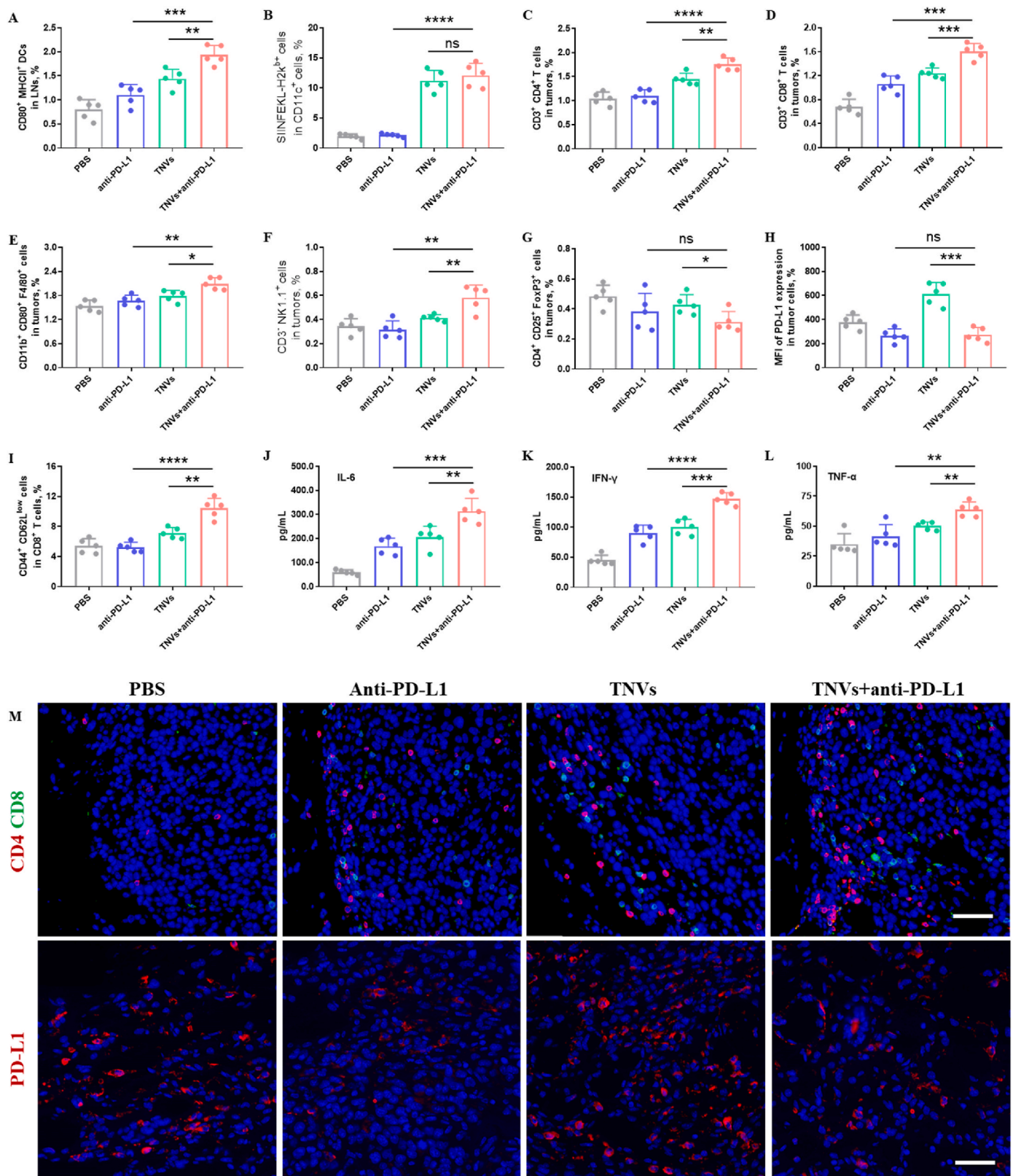
Fig. 7. Mechanism of anti-tumor treatment. Flow cytometry results of mature DCs (A) and Antigen cross-presentation of DCs in LNs (B). CD4$^+$ T cells (C), CD8$^+$ T cells (D), M1 macrophages (E), NK cells (F), Treg cells (G), and Mean fluorescence intensity (MFI) of PD-L1 (H) in tumors. Tregs in spleen (I). ELISA results of IL-6 (J), IFN-γ (K), and TNF-α (L). Immunofluorescence staining for CD8 (green), CD4 (red) and PD-L1 (red) in tumor slices (M). Scale bar = 50 μm *p < 0.05, **p < 0.01, ***p < 0.001, ****p < 0.0001, ns = not significant. (For interpretation of the references to colour in this figure legend, the reader is referred to the Web version of this article.)

Notably, the inhibitory combination treatment group exhibited upregulated levels of several pro-inflammatory cytokines, including IL-6 (Fig. 7J), IFN-γ (Fig. 7K), and TNF-α (Fig. 7L). This upregulation likely resulted from the efficient activation of anti-tumor immune cells and the overall immune system of the body. Furthermore, the increased cytokine secretion facilitated the recruitment and activation of immune cells. In essence, the intricate network of immune cells and cytokines within the body promotes and enhances each other's functions, ultimately leading to effective anti-tumor outcomes.

Immunofluorescence is a valuable technique for visualizing and quantifying cell markers and immune cells within tissues [47]. In our analysis, we examined the infiltration of CD4$^+$ T cells and CD8$^+$ T cells in tumor tissues. Consistent with flow cytometry results, we observed a significant increase in the number of T cell infiltrations in the combined treatment group (Fig. 7M). Additionally, the PD-L1 expression in tumors obviously increased after TNVs treatment, while introduction of
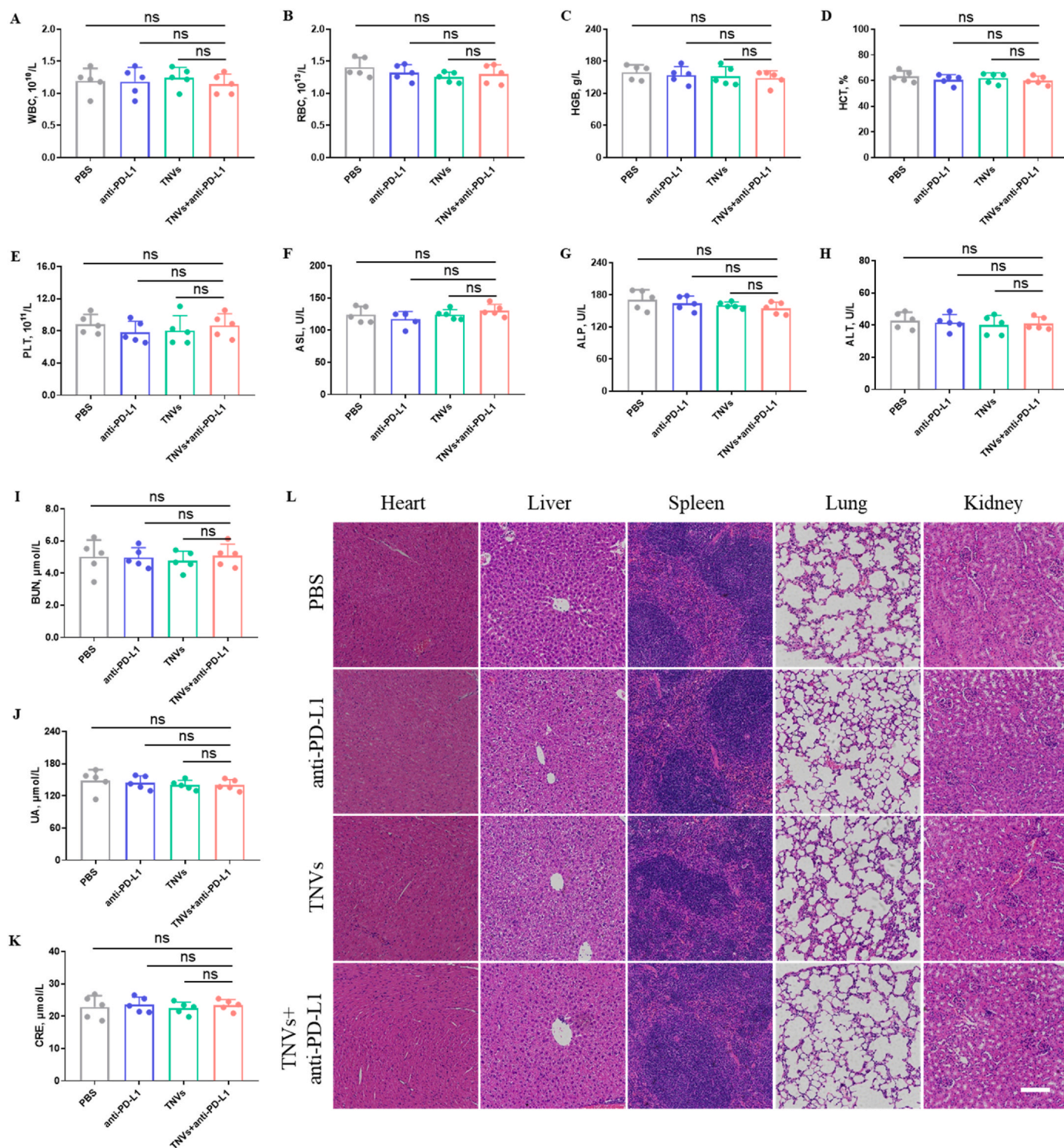

Fig. 8. Biological safety analysis after anti-tumor treatment. The routine blood test of WBC (A), RBC (B), HGB (C), HCT (D), and PLT (E). ELISA results of liver function indexes, including AST (F), ALP (G), and ALT (H). ELISA results of kidney function indexes, including BUN (I), UA (J), and CRE (K). H&E staining of the vital organs (L), scale bar = 200 μm ns = not significant.

anti-PD-L1 antibody treatment resulted in a marked reduction in PD-L1 protein expression in tumor tissues (Fig. 7M). We further supplemented and validated the expression of PD-L1 protein in tumor tissues after various treatments by Western blot. Consistent with the previous results of flow cytometry and immunofluorescence, the expression of PD-L1 in tumor tissue was increased after TNVs treatment, while the expression of PD-L1 in tumor tissue was significantly reduced after treatment with anti-PD-L1 antibody (Fig. S19). This reduction indicates that the immune tolerance microenvironment within tumors has been alleviated, thereby enhancing the specific cytotoxic activity of CTLs against tumor cells.

3.8. Biological safety analysis

Biological safety analysis is crucial to assess the impact of nanovaccines or other therapeutics on the immune system, organs, and cells. By monitoring blood biochemical indices, hepatic and renal toxicity indices, and performing histopathological examination, researchers can identify adverse effects or toxicities that may arise from anti-tumor therapy [48]. After treatment, blood samples were collected for routine blood tests and blood chemistry analysis. The results revealed no significant changes in the detected indicators across all treatment groups, including WBC (Fig. 8A), RBC (Fig. 8B), HGB (Fig. 8C), HCT (Fig. 8D), PLT (Fig. 8E), AST (Fig. 8F), ALP (Fig. 8G), ALT (Fig. 8H), BUN (Fig. 8I), UA (Fig. 8J), and CRE (Fig. 8K). Additionally, the body weights of mice in all treatment groups remained stable during treatment, further confirming the biosafety of the treatment strategy (Fig. S20). Furthermore, pathological changes in vital organs such as the heart, liver, spleen, lung, and kidney were analyzed using H&E staining and microscopic observation. The H&E staining results indicated that all these vital organs appeared normal across different treatment groups (Fig. 8L). These normal staining patterns suggest that the tissue architecture, cell morphology, and nuclear integrity are preserved, indicating that the administered treatments did not cause any overt histopathological damage or changes to the mouse organs. However, comprehensive safety assessments should always consider additional parameters and techniques to ensure the overall safety profile of the treatment before further clinical application.

Moreover, we augmented our investigation by evaluating the long-term safety in vivo. Specifically, the targeted nanovaccines were administered intramuscularly on days 0, 7, and 14. After a duration of 45 days, blood samples were collected for comprehensive blood biochemistry analyses. As depicted in Fig. S21, the blood routine test revealed no significant differences in WBC, RBC, and PLT counts between the TNVs group and the PBS-treated group. Furthermore, the assessment of liver function markers, including AKP, AST, and ALT, as well as kidney function-related biomarkers, such as UA, BUN, and CRE, revealed no significant discrepancies between the PBS and TNVs groups. These findings underscore the absence of significant long-term toxicity associated with TNVs in vivo.

4. Conclusions

In summary, we employed microfluidics technology to develop APC-targeted mRNA nanovaccines, ensuring efficient delivery of antigen-encoding mRNA to APCs for induction of tailored anti-tumor immune responses. This targeted delivery approach offers a promising avenue for safer, effective, and personalized vaccines against a range of diseases. The targeted nanovaccines, TNVs, exhibited a narrow particle size distribution, ensuring consistent and efficient antigen delivery. Their APC targeting capability enabled antigen presentation and immune activation more effectively than non-targeted vaccines. This led to enhanced mRNA gene expression in APCs, crucial for initiating and amplifying the immune response. Both in vitro and in vivo studies demonstrated the immunogenic potency of the targeted nanovaccines, eliciting robust immune responses that effectively suppressed tumor growth. Notably,

the nanovaccines achieved high levels of gene expression in vivo, further validating their therapeutic potential. Moreover, when combined with anti-PD-L1 antibodies, the nanovaccines exhibited a synergistic anti-tumor effect. This synergy was attributed to the antibodies' ability to overcome immune suppression and enhance T-cell activity, coupled with the immunogenic properties of the nanovaccines. Looking ahead, mRNA nanovaccine-based anti-tumor therapy holds great promise for the development of more effective and personalized cancer treatments. While tumor mRNA vaccines offer immense potential in cancer immunotherapy, they still face challenges in terms of target specificity, delivery, immunogenicity, manufacturing, and regulatory approval. Ongoing research and technological advancements are expected to address these challenges and pave the way for the clinical application of tumor mRNA vaccines. Future research ought to concentrate on refining the design and administration of nanovaccines, aiming to boost their immunogenicity and antitumor effectiveness. Additionally, it is imperative to investigate their potential for integration with other immunotherapies.

CRediT authorship contribution statement

Chengyan Jin: Writing – original draft, Methodology, Investigation, Formal analysis. **Yan Zhang:** Methodology, Investigation, Funding acquisition, Formal analysis. **Baofeng Li:** Software, Methodology. **Tianci Gao:** Investigation, Formal analysis. **Bin Wang:** Writing – review & editing, Supervision, Funding acquisition. **Peiyan Hua:** Writing – review & editing, Supervision, Project administration, Funding acquisition.

Declaration of competing interest

The authors declare that they have no known competing financial interests or personal relationships that could have appeared to influence the work reported in this paper.

Data availability

Data will be made available on request.

Appendix A. Supplementary data

Supplementary data to this article can be found online at https://doi.org/10.1016/j.mtbio.2024.101136.

References

[1] R.L. Siegel, K.D. Miller, H.E. Fuchs, A. Jemal, Cancer statistics, Ca-Cancer J Clin 72 (1) (2022) 7–33, 2022.

[2] M. McNutt, Cancer immunotherapy, Science 342 (6165) (2013) 1417, 1417.

[3] R.T. Shroff, P. Chalasani, R. Wei, D. Pennington, G. Quirk, M.V. Schoenle, K. L. Peyton, J.L. Uhrlaub, T.J. Ripperger, M. Jergovic, S. Dalgai, A. Wolf, R. Whitmer, H. Hammad, A. Carrier, A.J. Scott, J. Nikolich-Zugich, M. Worobey, R. Sprissler, M. Dake, B.J. LaFleur, D. Bhattacharya, Immune responses to two and three doses of the BNT162b2 mRNA vaccine in adults with solid tumors, Nat. Med. 27 (11) (2021) 2002–2011.

[4] C.H. Kim, E.S. Lee, H. Ko, S. Son, S.H. Kim, C.H. Lee, H.K. Na, J.M. Shin, J.H. Park, Stimuli-responsive polymeric nanomedicine for enhanced cancer immunotherapy, Chem. Mater. 36 (3) (2024) 1088–1112.

[5] I. Rana, J. Oh, J. Baig, J.H. Moon, S. Son, J. Nam, Nanocarriers for cancer nano-immunotherapy, Drug Deliv Transl Re 13 (7) (2023) 1936–1954.

[6] J. Chen, H.P. Fang, Y.Y. Hu, J.Y. Wu, S.J. Zhang, Y.J. Feng, L. Lin, H.Y. Tian, X. S. Chen, Combining mannose receptor mediated nanovaccines and gene regulated PD-L1 blockade for boosting cancer immunotherapy, Bioact. Mater. 7 (2022) 167–180.

[7] X. Liu, Y. Cheng, Y. Mu, Z.H. Zhang, D. Tian, Y.P. Liu, X.J. Hu, T. Wen, Diverse drug delivery systems for the enhancement of cancer immunotherapy: an overview, Front. Immunol. 15 (2024).

[8] M.J. Lin, J. Svensson-Arvelund, G.S. Lubitz, A. Marabelle, I. Melero, B.D. Brown, J. D. Brody, Cancer vaccines: the next immunotherapy frontier, Nat Cancer 3 (8) (2022) 911–926.

[9] Y.Y. Hu, L. Lin, J. Chen, A. Maruyama, H.Y. Tian, X.S. Chen, Synergistic tumor immunological strategy by combining tumor nanovaccine with gene-mediated extracellular matrix scavenger, Biomaterials 252 (2020) 120114.

[10] S.X. Li, J. Wu, X.P. Li, J.T. Chen, C.X. Wang, Biomaterial-enhanced cancer vaccines, Mater. Des. 218 (2022) 110720.

[11] A.J. Muller, S. Thomas, G.C. Prendergast, A brief overview of cancer vaccines, Cancer J. 29 (1) (2023) 34–37.

[12] Y. Hu, S. Gao, H. Lu, S. Tan, F. Chen, Y. Ke, J.Y. Ying, A self-immolative DNA nanogel vaccine toward cancer immunotherapy, Nano Lett. 23 (21) (2023) 9778–9787.

[13] L.R. Baden, H.M. El Sahly, B. Essink, K. Kotloff, S. Frey, R. Novak, D. Diemert, S. A. Spector, N. Rouphael, C.B. Creech, J. McGettigan, S. Khetan, N. Segall, J. Solis, A. Brosz, C. Fierro, H. Schwartz, K. Neuzil, L. Corey, P. Gilbert, H. Janes, D. Follmann, M. Marovich, J. Mascola, L. Polakowski, J. Ledgerwood, B.S. Graham, H. Bennett, R. Pajon, C. Knightly, B. Leav, W.P. Deng, H.H. Zhou, S. Han, M. Ivarsson, J. Miller, T. Zaks, C.S. Grp, Efficacy and safety of the mRNA-1273 SARS-CoV-2 vaccine, N. Engl. J. Med. 384 (5) (2021) 403–416.

[14] Y.X. Liu, Q.J. Yan, Z.Y. Zeng, C.M. Fan, W. Xiong, Advances and prospects of mRNA vaccines in cancer immunotherapy, Bba-Rev Cancer 1879 (2) (2024) 189068.

[15] S. Dong, Z. Feng, R. Ma, T. Zhang, J. Jiang, Y. Li, Y. Zhang, S. Li, X. Liu, X. Liu, H. Meng, Engineered design of a mesoporous silica nanoparticle-based nanocarrier for efficient mRNA delivery in vivo, Nano Lett. 23 (6) (2023) 2137–2147.

[16] H. Zhao, S. Ma, Y. Qi, Y. Gao, Y. Zhang, M. Li, J. Chen, W. Song, X. Chen, A polyamino acid-based phosphatidyl polymer library for in vivo mRNA delivery with spleen targeting ability, Mater. Horiz. 11 (11) (2024) 2739–2748.

[17] Z.Y. Tu, Q. Yu, R.Y. Wu, M. Meng, X.Y. Guo, J. Chen, Z.H. Tang, K. Hao, H.Y. Tian, X.S. Chen, High-Throughput screening of polymer library for mRNA tumor vaccine carriers with innate adjuvant properties, Chem. Mater. 36 (5) (2024) 2473–2482.

[18] A. Papachristofilou, M.M. Hipp, U. Klinkhardt, M. Früh, M. Sebastian, C. Weiss, M. Pless, R. Cathomas, W. Hilbe, G. Pall, T. Wehler, J. Alt, H. Bischoff, M. Geissler, F. Griesinger, K.J. Kallen, M. Fotin-Mleczek, A. Schroder, B. Scheel, A. Muth, T. Seibel, C. Stosnach, F. Doener, H.S. Hong, S.D. Koch, U. Gnad-Vogt, A. Zippelius, Phase Ib evaluation of a self-adjuvanted protamine formulated mRNA-based active cancer immunotherapy, BI1361849 (CV9202), combined with local radiation treatment in patients with stage IV non-small cell lung cancer, J Immunother Cancer 7 (2019) 1–14.

[19] U. Sahin, K. Karikó, Ö. Türeci, mRNA-based therapeutics - developing a new class of drugs, Nat. Rev. Drug Discov. 13 (10) (2014) 759–780.

[20] N. Xie, G.B. Shen, W. Gao, Z. Huang, C.H. Huang, L. Fu, Neoantigens: promising targets for cancer therapy, Signal Transduct Tar 8 (1) (2023) 9.

[21] A. Ablasser, J.L. Schmid-Burgk, I. Hemmerling, G.L. Horvath, T. Schmidt, E. Latz, V. Hornung, Cell intrinsic immunity spreads to bystander cells via the intercellular transfer of cGAMP, Nature 503 (7477) (2013) 530–534.

[22] W. Xie, D.J. Patel, Structure-based mechanisms of 2′3′-cGAMP intercellular transport in the cGAS-STING immune pathway, Trends Immunol. 44 (6) (2023) 450–467.

[23] L. Tan, X. Sun, Recent advances in mRNA vaccine delivery, Nano Res. 11 (10) (2018) 5338–5354.

[24] M.P. Lokugamage, Z.B. Gan, C. Zurla, J. Levin, F.Z. Islam, S. Kalathoor, M. Sato, C. D. Sago, P.J. Santangelo, J.E. Dahlman, Mild innate immune activation overrides efficient nanoparticle-mediated RNA delivery, Adv. Mater. 32 (1) (2020) 1904905.

[25] C. Liu, M. Wang, H.Y. Zhang, C.Y. Li, T.S. Zhang, H. Liu, S. Zhu, J. Chen, Tumor microenvironment and immunotherapy of oral cancer, Eur. J. Med. Res. 27 (1) (2022) 198.

[26] S. Rajbhandary, H. Dhakal, S. Shrestha, Tumor immune microenvironment (TIME) to enhance antitumor immunity, Eur. J. Med. Res. 28 (1) (2023) 169.

[27] P. Sadhukhan, T.Y. Seiwert, The role of macrophages in the tumor microenvironment and tumor metabolism, Semin. Immunopathol. 45 (2) (2023) 187–201.

[28] B.Z. Lv, Y.P. Wang, D.J. Ma, W. Cheng, J. Liu, T. Yong, H. Chen, C. Wang, Immunotherapy: reshape the tumor immune microenvironment, Front. Immunol. 13 (2022) 844142.

[29] S.J. Zhang, Y.J. Feng, M. Meng, Z. Li, H.X. Li, L. Lin, C.A. Xu, J. Chen, K. Hao, Z. H. Tang, H.Y. Tian, X.S. Chen, A generally minimalist strategy of constructing biomineralized high-efficiency personalized nanovaccine combined with immune checkpoint blockade for cancer immunotherapy, Biomaterials 289 (2022) 121794.

[30] L.N. Zheng, X. Yang, Y.F. Wei, J. You, H.W. Li, J.F. Liao, C. Yi, Advanced materials for management of immune-related adverse events induced by immune checkpoint inhibitors, Mater. Des. 219 (2022) 110738.

[31] Y. Zhang, C. Chen, M. Su, J. Wang, C. Li, X. Yang, Hydrophobization of ribonucleic acids for facile systemic delivery and multifaceted cancer immunotherapy, Nano Lett. 24 (4) (2024) 1376–1384.

[32] E.J. Lipson, C.G. Drake, Ipilimumab: an anti-CTLA-4 antibody for metastatic melanoma, Clin. Cancer Res. 17 (22) (2011) 6958–6962.

[33] E.D. Deeks, Nivolumab: a review of its use in patients with malignant melanoma, Drugs 74 (11) (2014) 1233–1239.

[34] C.Y. Jin, Y. Zhang, G.X. Zhang, B. Wang, P.Y. Hua, Combination of GNRs-PEI/ cGAMP-laden macrophages-based photothermal induced in situ tumor vaccines and immune checkpoint blockade for synergistic anti-tumor immunity, Biomater. Adv. 133 (2022) 112603.

[35] Y.Z. Min, K.C. Roche, S.M. Tian, M.J. Eblan, K.P. McKinnon, J.M. Caster, S.J. Chai, L.E. Herring, L.Z. Zhang, T. Zhang, J.M. DeSimone, J.E. Tepper, B.G. Vincent, J. S. Serody, A.Z. Wang, Antigen-capturing nanoparticles improve the abscopal effect and cancer immunotherapy, Nat. Nanotechnol. 12 (9) (2017) 877–882.

[36] L. Zhao, W. Jin, J.G. Cruz, N. Marasini, Z.G. Khalil, R.J. Capon, W.M. Hussein, M. Skwarczynski, I. Toth, Development of polyelectrolyte complexes for the delivery of peptide-based subunit vaccines against group A Streptococcus, Nanomaterials 10 (5) (2020) 823.

[37] Y.Z. Chen, J.J. Zhu, J.S. Ding, W.H. Zhou, Recent progress of vaccines administration via microneedles for cancer immunotherapy, Chinese Chem Lett 35 (3) (2024) 108706.

[38] J.F. Liu, J. Wang, Q.Q. Zhu, C.Q. Yu, J.R. Yin, L.P. Zheng, A. Li, Mannosylated PEGylated-polyethyleneimine as efficient CpG oligodeoxynucleotide carriers for efficient dendritic cell targeting delivery and activation, J. Biomed. Nanotechnol. 15 (7) (2019) 1454–1467.

[39] L. Miao, Y. Zhang, L. Huang, mRNA vaccine for cancer immunotherapy, Mol. Cancer 20 (1) (2021) 1–23.

[40] Y.L. Vishweshwaraiah, N.V. Dokholyan, mRNA vaccines for cancer immunotherapy, Front. Immunol. 13 (2022) 1–23.

[41] B. Jneid, A. Bochnakian, C. Hoffmann, F. Delisle, E. Djacoto, P. Sirven, J. Denizeau, C. Sedlik, Y. Gerber-Ferder, F. Fiore, R. Akyol, C. Brousse, R. Kramer, I. Walters, S. Carlioz, H. Salmon, B. Malissen, M. Dalod, E. Piaggio, N. Manel, Selective STING stimulation in dendritic cells primes antitumor T cell responses, Sci Immunol 8 (79) (2023) eabn6612.

[42] J.Y. Wu, Z.P. Guo, W.D. Ni, Y.J. Feng, X.Y. Guo, M. Meng, Y.A. Yuan, L. Lin, J. Chen, H.Y. Tian, X.S. Chen, Novel cocktail therapy based on a nanocarrier with an efficient transcytosis property reverses the dynamically deteriorating tumor microenvironment for enhanced immunotherapy, Nano Lett. 22 (17) (2022) 7220–7229.

[43] T. Li, L.S. Guo, J.X. Li, X.Y. Mu, L.J. Liu, S.L. Song, N.B. Luo, Q. Zhang, B. Zheng, G. Q. Jin, Precision USPIO-PEG-SLeS nanotheranostic agent targeted photothermal therapy for enhanced anti-PD-L1 immunotherapy to treat immunotherapy resistance, Int. J. Nanomed. 19 (2024) 1249–1272.

[44] Y.B. Zhang, X.C. Hou, S. Du, Y.E. Xue, J.Y. Yan, D.D. Kang, Y.C. Zhong, C. Wang, B. B. Deng, D.W. McComb, Y.Z. Dong, Close the cancer-immunity cycle by integrating lipid nanoparticle-mRNA formulations and dendritic cell therapy, Nat. Nanotechnol. 18 (11) (2023) 1364–1374.

[45] F.L. Huang, Q. Zhang, J. Xiao, X. Zhang, X.Z. Han, X. Shi, J. Hu, L. Li, X.P. Qian, Cancer cell membrane-coated gambogic acid nanoparticles for effective anticancer vaccination by activating dendritic cells, Int. J. Nanomed. 18 (2023) 2261–2273.

[46] V. Jurisic, Multiomic analysis of cytokines in immuno-oncology, Expert Rev Proteomic 17 (9) (2020) 663–674.

[47] Y. Severin, B.D. Hale, J. Mena, D. Goslings, B.M. Frey, B. Snijder, Multiplexed high-throughput immune cell imaging reveals molecular health-associated phenotypes, Sci. Adv. 8 (44) (2022) eabn5631.

[48] D. Liu, B. Deng, Z.R. Liu, B. Ma, X.G. Leng, D.L. Kong, T.J. Ji, L.X. Liu, Enhanced antitumor immune responses via a self-assembled carrier-free nanovaccine, Nano Lett. 21 (9) (2021) 3965–3973.